NASA TECHNICAL NOTE

NASA TN D-7723

NASA TN D-7723

(NASA-TN-D-7723) BOUNDARY-LAYER TRANSITION AND DISPLACEMENT THICKNESS EFFECTS ON ZERO-LIFT DRAG OF A SERIES OF POWER-LAW BODIES AT MACH 6 (NASA) 66 p HC $3.75

CSCL 20D H1/12

N74-32751

Unclas 48965

BOUNDARY-LAYER TRANSITION AND DISPLACEMENT-THICKNESS EFFECTS ON ZERO-LIFT DRAG OF A SERIES OF POWER-LAW BODIES AT MACH 6

by George C. Ashby, Jr., and Julius E. Harris

Langley Research Center

Hampton, Va. 23665

NATIONAL AERONAUTICS AND SPACE ADMINISTRATION • WASHINGTON, D. C. • SEPTEMBER 1974

1. Report No.	2. Government Accession No.	3. Recipient's Catalog No.
NASA TN D-7723		

4. Title and Subtitle	5. Report Date
BOUNDARY-LAYER TRANSITION AND DISPLACEMENT-THICKNESS EFFECTS ON ZERO-LIFT DRAG OF A SERIES OF POWER-LAW BODIES AT MACH 6	September 1974
	6. Performing Organization Code
7. Author(s)	8. Performing Organization Report No.
George C. Ashby, Jr., and Julius E. Harris	L-9646
	10. Work Unit No.
9. Performing Organization Name and Address	502-37-01-04
NASA Langley Research Center Hampton, Va. 23665	11. Contract or Grant No.
	13. Type of Report and Period Covered
12. Sponsoring Agency Name and Address	Technical Note
National Aeronautics and Space Administration Washington, D.C. 20546	14. Sponsoring Agency Code

15. Supplementary Notes

16. Abstract

Wave and skin-friction drag have been numerically calculated for a series of power-law bodies at a Mach number of 6 and Reynolds numbers, based on body length, from 1.5×10^6 to 9.5×10^6. Pressure distributions were computed on the nose by the inverse method and on the body by the method of characteristics. These pressure distributions and the measured locations of boundary-layer transition were used in a nonsimilar-boundary-layer program to determine viscous effects. A coupled iterative approach between the boundary-layer and pressure-distribution programs was used to account for boundary-layer displacement-thickness effects. The calculated-drag coefficients compared well with previously obtained experimental data.

17. Key Words (Suggested by Author(s))	18. Distribution Statement
Hypersonic flow Minimum drag Boundary-layer displacement thickness	Unclassified – Unlimited Star Category 12

19. Security Classif. (of this report)	20. Security Classif. (of this page)	21. No. of Pages	22. Price*
Unclassified	Unclassified	64	$3.75

*For sale by the National Technical Information Service, Springfield, Virginia 22151

BOUNDARY-LAYER TRANSITION AND DISPLACEMENT-THICKNESS EFFECTS ON ZERO-LIFT DRAG OF A SERIES OF POWER-LAW BODIES AT MACH 6

By George C. Ashby, Jr., and Julius E. Harris
Langley Research Center

SUMMARY

The influence of viscous effects on the zero-lift drag of a series of power-law bodies has been examined analytically and experimentally at a Mach number of 6. Bodies constrained to length-diameter ratios of 6.63 with values of the power-law exponent in the shape equation of 0.25, 0.50, 0.60, 0.667, 0.75, and 1.00 were studied. The pressure drag of each body was computed by using the method of characteristics, and the skin friction was computed by using a numerical solution of the compressible boundary layer with the local flow properties predicted by the method of characteristics. The location of boundary-layer transition on the models was determined from phase-change-coating heat-transfer measurements, and the effects of transition and boundary-layer displacement were included in the calculations. The calculated drags were compared with experimental results obtained at a Mach number of 6 over a Reynolds number range, based on body length, of 1.50×10^6 to 9.50×10^6. The analysis showed that the exponent for minimum drag with either inviscid or fully laminar flow was approximately 0.667. However, if boundary-layer transition existed on the bodies, the exponent for minimum drag was lower. For the experimental results at the higher Reynolds numbers, boundary-layer transition occurred, and the resulting exponent for minimum drag was approximately 0.6.

The effect of displacement thickness on total drag was significant but was nearly constant for all the bodies exerting only a minor influence in the determination of the body with minimum zero-lift drag. For the present tests, the boundary-layer displacement-thickness effect on total drag was as high as 9 percent with the major contribution coming from wave drag.

INTRODUCTION

Early studies, typified by references 1 and 2, which were conducted to determine the body and/or wing profiles with minimum zero-lift drag considered only the inviscid drag and used approximate pressure laws. Subsequent investigators included the effects of

skin friction but in a simplified manner. (See, for example, ref. 3.) The results from such basic investigations, however, have been useful design guides and have been shown to be generally applicable under lifting as well as zero-lift conditions (refs. 4 and 5).

More recently, with the focus of attention on the advanced space transportation systems, the practical application of body shaping to improve hypersonic performance has received greater impetus, and some refined results have been obtained. For example, in reference 6 a critical assessment of the pressure laws used in previous optimization studies (primarily the Newton pressure laws) revealed that more exact pressure laws, such as the method of characteristics, defined optimum bodies which had more volume forward than previous studies had shown. Furthermore, experimental data for a series of power-law bodies obtained at a Mach number of 6 over a large Reynolds number range in support of reference 6 indicated that a blunter body than the one predicted by the exact pressure laws would have the minimum zero-lift drag. This result was attributed to the variation of boundary-layer transition between the bodies at the test flow conditions and promoted the current study.

The purpose of the present investigation was to determine the influence of viscous effects on the minimum zero-lift drag. Accordingly, calculations were made of skin-friction and boundary-layer displacement effects on a series of power-law bodies which were tested at a Mach number of 6 and reported in references 6 and 7. In the reference tests the condition of the boundary layer was not established, but the range of Reynolds numbers was large enough for the boundary layer to vary from laminar over the entire body to a laminar-transitional-turbulent state over the entire body. For the present study, the boundary-layer transition location was determined on reproductions of the force models by phase-change-coating heat-transfer measurements at zero angle of attack for Reynolds numbers corresponding to those of the reference test. (See refs. 6 and 7.) These measured transition locations along with a pressure distribution calculated by the inverse method for the nose and the method of characteristics for the body were used in a nonsimilar-boundary-layer program to compute the skin-friction and wave-drag coefficients on each body. An iterative approach was used to couple the boundary-layer and the pressure-distribution programs to account for boundary-layer displacement effects. The computed results are presented and compared with experimental drag coefficients herein.

SYMBOLS

Measurements and calculations were made in the U.S. Customary Units. They are presented herein in the International System of Units (SI) with the equivalent values given in the U.S. Customary Units.

A	model base area, meters^2 (feet^2)
C_D	drag coefficient, $\frac{\text{Drag}}{qA}$
$C_{D,f}$	total skin-friction-drag coefficient, $\frac{\text{Total skin-friction drag}}{qA}$
$C_{D,T}$	total-drag coefficient, sum of wave and skin-friction drag, $\frac{\text{Total drag}}{qA}$
$C_{D,W}$	wave-drag coefficient, $\frac{\text{Wave drag}}{qA}$
C_f	local skin-friction coefficient
C_p	pressure coefficient, $\frac{p_e - p_\infty}{q}$
l	model length, centimeters (feet)
n	exponent in shape equation for power-law bodies, $\frac{r}{R} = \left(\frac{x}{l}\right)^n$ (see fig. 1)
p_e	body surface pressure, newtons/meter^2 (pounds/foot^2)
p_∞	free-stream static pressure, newtons/meter^2 (pounds/foot^2)
q	free-stream dynamic pressure, newtons/meter^2 (pounds/foot^2)
R	base radius of power-law bodies, centimeters (feet)
$R_{\infty,l}$	Reynolds number based on free-stream properties and model length
r,x	coordinates on meridian curve of power-law body, centimeters (feet) (see fig. 1)
S	distance along body surface, centimeters (feet)
U_{ej}	velocity at edge of boundary layer, centimeters/second (feet/second)
$x_{t,f}$	end of boundary-layer transition

$x_{t,i}$ beginning of boundary-layer transition

δ inclination of body surface relative to free stream, degrees

δ^* boundary-layer displacement thickness, centimeters (feet)

MEASURED LOCATIONS OF BOUNDARY-LAYER TRANSITION

Models

The heat-transfer models used in this investigation were cast reproductions of the force models (ref. 7) and are shown in figure 1. The six power-law bodies, which are defined by $\frac{r}{R} = \left(\frac{x}{l}\right)^n$ with $n = 0.25, 0.50, 0.60, 0.667, 0.75$, and 1.00, were circular in cross section, had a fineness ratio of 6.63, and were constrained for constant length and base diameter. Each model had an aluminum nose and a high-temperature epoxy plastic body. The measured coordinates of the heat-transfer models are within 0.040 cm of those for the force tests in reference 6. The noses of the heating models were individually shaped to match those of the force models.

Wind Tunnel and Tests

The transition measurements were conducted in the same tunnel as the force tests of reference 7, the Langley 20-inch Mach 6 tunnel. It is a blowdown type exhausting to either atmosphere or vacuum with an operating range of stagnation pressures from 3 to 35 atmospheres (0.304 to 3.55 MN/m^2) and stagnation temperatures up to 589 K. The general details of the tunnel, along with schematic drawings, are presented in reference 8.

The location of boundary-layer transition was measured on each body, by using a phase-change-coating technique described in reference 9, at five Reynolds numbers, from 1.50×10^6 to 9.50×10^6 based on model length. Four of the Reynolds numbers matched those of the reference force tests. Since transition did not occur on any of the bodies at the lowest Reynolds number, an additional intermediate Reynolds number was selected to give a more complete trend. All tests were conducted at zero angle of attack and sideslip.

Method of Determining Transition

Transition could be observed visually on these models because of heat-rate variations between laminar, transitional, and turbulent boundary-layer regions. (See fig. 2.) Note that the light region in the photograph is the unmelted area. In the phase-change technique the heating rate is inversely proportional to the time required to melt the coating. Progressing rearward from the apex of the model nose, the heating rate decreases

through the laminar region and becomes a minimum at the start of transition. The rate increases through the transition region until fully turbulent flow is established and then decreases at a relatively low rate in the turbulent region. Under these conditions, a coating which melts at a specific temperature when applied uniformly to the model will begin to melt at the nose and then at or near the rear, depending on whether or not transition is completed on the body. The two melting regions approach each other and meet at the initial transition point, which is the last place the coating melts. The series of photographs in figure 2 show an example of the melting sequence.

For each test, the model was coated and mounted on a tunnel injection strut in the retracted position. After starting the tunnel and setting the flow conditions to the desired Reynolds numbers, the model was injected and observed visually until the phase-change process was complete. The time histories of the phase change of the coating were recorded with motion-picture cameras on both the top and right side of the models. The location of the beginning of transition (last melt point) and, where possible, the end of transition (first rearward melt point) were scaled from those pictures.

Locations of Boundary-Layer Transition

Typical peripheral distribution of the beginning of transition obtained from the phase-change-coating tests at $\alpha = 0^{\circ}$ are presented in figure 3, and the values used in the boundary-layer calculations are shown in figure 4. The average values were used because transition occurred at a smaller value of $x_{t,i}$ on top than on the side and, in general, was not uniform about the body. Similar results were reported in references 10 and 11. For the present paper, the variation was less than 20 percent of the model length and could have been caused by any of several factors. For example, model irregularities could alter the location of boundary-layer transition. In reference 11 a deliberate nose-tip offset of 0.1 percent of the tip length (0.005 cm) caused transition location to vary circumferentially about the body by 10 to 35 percent of the length. Nonuniform distribution of the phase-change coating or small flow angularity could also cause an asymmetric distribution of transition location.

The variations in the location of the beginning of transition with Reynolds number for the five bodies in figure 4 are reasonably well behaved and do not exhibit any large anomalies. The apparent reversal of transition in the data for the bodies with $n = 0.60$ and 0.75 at the higher Reynolds number is believed to be associated with nonuniformity of transition around the body. No reason is known for such transition reversal under these flow variations; therefore, the curve presented in figure 4 for $n = 0.60$ was faired without reversal. Calculations showed that, for the body with $n = 0.60$ at a Reynolds number of 9.5×10^6 and a transition-location variation from 52 to 69 percent of the body length, the skin-friction drag coefficient would vary only about 0.001, which is within the accuracy

of the measured drag coefficients. Thus, the difference between the curve as shown and a fairing through all the points was found to have an insignificant effect on skin-friction-drag coefficients.

The distance to transition from the nose varies inversely with the power-law exponent (directly with nose bluntness, i.e., bluntness delays transition), which is in agreement with the results presented in reference 12. As the Reynolds number increases, transition moves forward, but the rate of forward movement is a direct function of n (inverse function of nose bluntness). At the higher Reynolds numbers of these tests, the rate of forward movement approaches zero for the bodies with $n = 0.60$ to 0.75; whereas, the location of transition on the body with $n = 1.00$ is more linear with Reynolds number. The difference in the variation of transition location between the body with $n = 1.00$ and the others at the high Reynolds numbers is not understood, but similar results were reported for a slightly blunted 5° half-angle cone at a Mach number of 8 in reference 13.

The end of transition could not be positively identified for all cases (i.e., the beginning of turbulent flow did not occur on the body); those for which it could be identified are shown in figure 5. The ratio of the location of the end of transition to the location of the beginning of transition varies from approximately 1.2 to 1.7. Because no systematic variation exists, a nominal value of 1.5, represented by the dashed line, was used for all calculations. A value of 1.5 for the average extent of boundary-layer transition is at the lower end of the range of values mentioned in reference 14 for a large amount of data.

VISCOUS EFFECTS ON POWER-LAW BODY FOR MINIMUM ZERO-LIFT DRAG

Effect of Boundary-Layer Transition

The variation of the calculated skin-friction, wave, and total-drag coefficients with power-law exponent for the bodies at the four test Reynolds numbers are presented in figure 6. The procedure used to compute the total-drag coefficients for the power-law bodies, including the effects of boundary-layer transition and displacement thickness, is presented in the appendix. Note that the measured locations of transition were used in the calculations. By considering wave drag only, the body with minimum drag would have an exponent n of approximately 0.667 (middle group of curves in fig. 6). This body is blunter than that predicted by Eggers et al. and by Miele ($n = 0.75$) in references 1 and 3, respectively, by using Newton's pressure law $\left(C_p \propto \sin^2 \delta\right)$. The difference in the bodies for minimum drag between this investigation and those of Eggers and Miele is attributed to the difference in pressure laws. This investigation used the method of characteristics, and Eggers and Miele used Newton's pressure law. A comprehensive discussion of the

effects of several pressure laws and methods used to predict minimum wave-drag shapes is contained in reference 6.

When viscous effects are included $\left(C_{D,T}\right.$ in fig. 6$\left.\right)$, the exponent for minimum drag remains near 0.667 until the Reynolds number increases beyond 4.37×10^6, above which it shifts towards a value of 0.60. This trend is caused by the variation of boundary-layer transition with Reynolds number for each power-law body (fig. 4). The location of transition onset from the body nose $x_{t,i}$ at a given Reynolds number varies inversely with the power-law exponent n (directly with bluntness, i.e., bluntness delays transition), while the rate of forward movement of transition location with Reynolds number $dx_{t,i}/dR_{\infty,l}$ varies directly with n. These divergent trends cause the increase in skin friction to be larger for the higher exponent bodies as Reynolds number increases and therewith the minimum total drag to shift towards the lower exponent, blunter bodies. Although these calculations include displacement thickness, it has little effect on the power-law body for minimum drag as is shown subsequently.

The results of figures 4 and 6 confirm and explain more completely the shift in minimum drag towards a blunter body exhibited by the experimental data for the same series of bodies at a Mach number of 6 and the higher Reynolds numbers (refs. 6 and 7). In the references the shift was correctly attributed to the variation of the location boundary-layer transition from body to body at a constant Reynolds number.

A comparison of the calculated values of total-drag coefficient with the experimental data is presented in figure 7. The height of symbols in the figure is representative of the experimental measuring accuracy, and the agreement between the measured and computed data for the majority of the points is within this accuracy. Of those points for which the measured and computed data do not agree, all but two are for the sharper bodies at the higher Reynolds numbers. If the location of transition for the bodies with $n = 0.667$ and 0.75 had been the linearly extrapolated value (21 percent of length in fig. 4) and for the body with $n = 1.00$ had been at 50 percent of the body length, then the calculated values of $C_{D,T}$ for $R_{\infty,l} = 9.5 \times 10^6$ would have been represented by the dashed-line curves in figure 7. Under these assumptions the agreement between the calculated values and the measured data is good. At $R_{\infty,l} = 6.42 \times 10^6$, the calculated-drag-coefficient value for the body with $n = 1.00$ can be adjusted to agree with the measured value by assuming that the location and the nondimensionalized extent of transition are 58 percent of body length and 2.0, respectively, instead of the measured values of 46 percent and 1.5. Similar assumptions would bring the data for the body with $n = 0.75$ at the same Reynolds number into agreement with experiment. This exercise indicates that the calculated data agree with the experimental data for reasonable assumptions of boundary-layer transition.

Effect of Boundary-Layer Displacement Thickness

Boundary-layer displacement thicknesses for each body are presented in figure 8 as a function of S/l at each of the test Reynolds numbers. The location of transition used in the calculations is indicated on each curve if transition occurred for that particular Reynolds number. When transition begins somewhat forward of the body base, a marked dip in δ^* is followed by a rapid increase. However, the maximum thickness never exceeds that for the completely laminar-flow case at the lowest Reynolds number. The scale at the right (fig. 8) is a measure of the displacement thickness at the base in percent of the base radius. For the conditions of this investigation, the displacement thickness at the base varies from approximately 4 to 12 percent of the base radius.

Effect on surface pressure.- The computed pressure distributions on each body with and without boundary-layer displacement effects at the highest and lowest Reynolds numbers are presented in figure 9. The plots arbitrarily terminate at the body station where the two pressure distributions appear to converge. These results indicate that the primary effect of displacement thickness on surface pressure is generally confined to the first 4 percent of the body length.

Effect on skin friction.- Skin-friction coefficients for each body with and without boundary-layer displacement effects are presented in figure 10 for the maximum and minimum test Reynolds numbers. These comparison plots were terminated, in general, prior to 1 percent of the body length because the effects were negligible beyond this region. This small effect is reflected in the less than 3-percent difference in the integrated values of viscous drag with and without displacement-thickness effects, as discussed in the next section. The distributions of the skin-friction coefficient, including the effect of boundary-layer displacement thickness are shown in figure 11. The location of transition used in the calculations is also indicated in figure 11 where appropriate.

Effect on drag.- The pressure and skin-friction distributions were integrated over the entire wetted surface to get the total drag for each body and each test Reynolds number. The change in drag coefficient due to boundary-layer displacement effects is observed to be nearly constant with power-law displacement at all Reynolds numbers (fig. 12), thereby indicating that boundary-layer displacement does not have a strong influence in determining the power-law body with the minimum zero-lift drag. The primary effect of displacement thickness is on the wave-drag coefficient (fig. 12(b)). This effect is more clearly evident in figure 13 where the changes in the total-drag-coefficient components due to displacement effects are plotted against the power-law exponent for the four Reynolds numbers. The increase in drag due to boundary-layer displacement ranges from 2 to 9 percent for total drag, 3 to 16 percent for wave drag, and below 3 percent for skin-friction drag. The level of the effect is, in general, an inverse function of Reynolds number.

Boundary-layer displacement effects on total drag reach a maximum at n near 0.5 (fig. 13(a)); whereas for wave drag they peak near a value of 0.6 (fig. 13(b)). The reduction in displacement effects beyond this peak is more abrupt for wave drag than for total drag. In both cases, however, the drop is tempered somewhat by increasing Reynolds number. Cross plots of the drag coefficients against Reynolds number (fig. 14) tend to obscure these anomalies and, in general, show an inverse variation of boundary-layer displacement effects with Reynolds number. The large increases in displacement effects for $n = 1.00$ at the higher Reynolds numbers is attributed to the earlier transition on that body.

CONCLUDING REMARKS

Wave and skin-friction-drag coefficients have been numerically calculated for a series of power-law bodies at a Mach number of 6 and Reynolds numbers, based on body length, from 1.5×10^6 to 9.5×10^6. These calculations were used to evaluate the impact of boundary-layer transition and displacement thickness in the determination of the power-law body with minimum drag. The calculated-drag results were compared with previously obtained experimental data.

The results of this investigation indicate that, when boundary-layer transition occurs, the body for minimum zero-lift drag can be blunter than when the boundary layer is fully laminar. This condition occurs because the location of transition at a given Reynolds number varies directly with nose bluntness, thereby causing the skin friction to decrease with nose bluntness and the minimum total drag to shift to a blunter body. The calculated values agree well with the experimental data.

The effect of displacement thickness on drag is significant but is nearly constant for all the bodies and therefore has very little influence in the determination of the body with minimum zero-lift drag. For the present tests, boundary-layer displacement-thickness effect is as high as 9 percent of the total drag.

The results from this investigation are applicable to the design of high-performance missiles and cruise and entry configurations at hypersonic speeds. For example, if at zero-lift, conditions for boundary-layer transition are encountered in flight, a blunter nose should be considered as a trade-off for improving aerodynamic performance as well as reducing aerodynamic heating. Furthermore, the boundary-layer displacement thickness is a sizable percentage of the body radius, varying from 4 to 12 percent at the base. The effect of boundary-layer displacement thickness on drag can also be sizable (up to 9 percent from this investigation) and should be included in performance calculations.

These results are also useful as a guide in the design of hypersonic missiles and cruise and entry vehicles for lifting conditions. Previous work has shown that for some cases body shapes for minimum wave drag at zero lift have the best performance under lifting conditions at hypersonic speeds. Analogously, the identification, in this paper, of blunt bodies for minimum drag at zero lift when the boundary layer is transitional should be applicable to the design of lifting cruise vehicles and entry configurations. For such applications, blunting for practical packaging and aerodynamic stability requirements might be less penalizing than indicated by previous studies.

Langley Research Center,
National Aeronautics and Space Administration,
Hampton, Va., June 25, 1974.

APPENDIX

DETERMINATION OF BOUNDARY-LAYER DISPLACEMENT EFFECTS ON WAVE AND SKIN-FRICTION DRAG

Procedure

The effect of boundary-layer displacement thickness on drag was determined by an iterative procedure diagramed in figure 15. Seven different computer programs were utilized with the iteration requiring three passes through five of the programs to obtain a solution.

To start the calculations, the inverse method for blunt-nose bodies at hypersonic speeds (ref. 15) was used to compute the surface pressures on the nose of a sphere and a paraboloid and the flow properties in the shock layer along a line normal to each of these nose shapes in the transonic flow region. This line is called a field data line in the reference. The sphere and paraboloid were fitted to the particular power-law body ($n < 1.00$) at the body slope of the field data line. The flow-field properties of the nose shape, which best matched that of the body nose shape, were used in the method-of-characteristics program of reference 16 to compute the pressure distribution over the remainder of the body. A curve-fit program using cubic spline functions was then applied to the complete pressure distribution. The coefficients of the equation from this pressure curve fit, the body coordinates from a body geometry program, and the measured location of boundary-layer transition were input to the nonsimilar-boundary-layer program of reference 17, which used the numerical technique reported in reference 18. In the latter program, the integrated wave and skin-friction drags as well as the boundary-layer properties were determined, and the coordinates for the body plus the displacement thickness were obtained.

The iteration procedure for displacement effects began with a program which determined an effective power-law body for the basic body enlarged by the boundary-layer displacement. This effective body was required because the boundary-layer displacement was somewhat nonuniform with transition present, and the method-of-characteristics program is difficult to use without a continuous surface slope. From this point, the calculation procedure looped back through the sphere or paraboloid nose match, the method-of-characteristics, the pressure curve-fit, and the boundary-layer programs. This loop was repeated until the velocity at the edge of the boundary layer agreed with that of the previous pass to within 1 percent. Agreement was accomplished in all cases after the third pass through the boundary-layer program.

For the body with $n = 1.00$ (cone), the initial pass used a constant surface pressure from the cone tables (ref. 19), the geometric parameters, and the measured transition

location in the boundary-layer program. In the subsequent iterations, the pressure distributions were obtained from a method-of-characteristics program, developed by Lillian R. Boney of NASA Langley Research Center, for the effective body with a conical nose.

Program Applicability

Blunt-body pressure.- The only exact nose match for the pressure calculations was the paraboloid to the body with $n = 0.50$. For all bodies with $0.50 \leq n < 1.00$, the paraboloid was the closest match; and the properties for the field data line from it were used in the method-of-characteristics calculation. The power-law body with the exact nose match to a sphere is $n = 0.413$; therefore, the spherical nose properties were used only for the pressure calculations for $n = 0.25$. The following table shows the maximum axial distances (normalized by body length) between the body nose and the nose of the paraboloid or sphere, which was matched to the body at the initial point of the method-of-characteristics solution for the initial pass, first iteration, and the second iteration:

n	$\Delta x/l$ for –		
	Initial pass	First iteration	Second iteration
0.25	-0.00330900	-0.00323000	-0.00323600
.50	.00000004	.00003130	.00003220
.60	.00000841	.00010470	.00014150
.667	.00003770	.00005440	.00005340
.75	.00000432	.00001010	.00000973

In all cases, the differences between the actual and calculated nose shapes is extremely small. All of the shapes fitted to the power-law bodies lie inside of the body except for the sphere fitted to the body with $n = 0.25$, which is somewhat blunter than a sphere.

Method-of-characteristics solution.- The method-of-characteristics solution extended the full body length for all cases except the body with $n = 0.75$, which covered only 5 percent of the body. However, comparison of this calculation with the pressure distribution obtained with the method-of-characteristics program of Lillian R. Boney, using a 45° starting cone, showed that the two became coincident at 0.007 percent of the body length from the nose; therefore, the two solutions were joined at this point to obtain the complete distribution.

Cubic spline curve fit of pressure distribution.- The cubic spline curve fit was performed on a cathode ray tube and involved shifting spline curve junction points until the

complete curve system was observed to conform to the pressure distribution. In the curve fits, from 9 to 16 junction points were utilized, depending on the slenderness of the body. Figure 16 shows some examples of the curve fit with the junction points identified by the vertical tick marks.

Boundary-layer program.- The numerical technique presented in reference 18 was used to solve the nonsimilar equations governing the laminar, transitional, and turbulent compressible flow over the power-law bodies. The turbulent boundary layer was represented by a two-layer concept with appropriate eddy-viscosity models used for each layer to replace the Reynolds stress term. A static turbulent Prandtl number model was used to relate the turbulent-heat-flux term in the energy equation to the Reynolds stress model. The mean properties in the transitional boundary layer were calculated by multiplying the eddy viscosity by an intermittency function based on the statistical production and growth of the turbulent spot in the transitional region of flow. The computer code and flow charts are presented in reference 17.

Effective-body program (Body + δ^*).- Before the procedure repeats, the last program determines an effective power-law body for the basic body with the boundary-layer displacement thickness superimposed. Several examples of this curve fit are shown in figure 17. The accuracy of representation varies inversely with nose bluntness; nonetheless, the representation in all cases is good.

REFERENCES

1. Eggers, A. J., Jr.; Resnikoff, Meyer M.; and Dennis, David H.: Bodies of Revolution Having Minimum Drag at High Supersonic Airspeeds. NACA Rep. 1306, 1957. (Supersedes NACA TN 3666.)

2. Drougge, Georg: Wing Sections With Minimum Drag at Supersonic Speeds. Rep. No. 26, Aero. Res. Inst. of Sweden (Stockholm), 1949.

3. Miele, Angelo, ed.: Theory of Optimum Aerodynamic Shapes. Academic Press, Inc., c.1965.

4. Spencer, Bernard, Jr.; and Fox, Charles H., Jr.: Hypersonic Aerodynamic Performance of Minimum-Wave-Drag Bodies. NASA TR R-250, 1966.

5. Spencer, Bernard, Jr.: Hypersonic Aerodynamic Characteristics of Minimum-Wave-Drag Bodies Having Variations in Cross-Sectional Shape. NASA TN D-4079, 1967.

6. Love, E. S.: Design of Bodies for Low Drag and High Performance in Practical Hypersonic Flight. Performance and Dynamics of Aerospace Vehicles, NASA SP-258, 1971, pp. 103-174.

7. Ashby, George C., Jr.: Longitudinal Aerodynamic Performance of a Series of Power-Law and Minimum-Wave-Drag Bodies at Mach 6 and Several Reynolds Numbers. NASA TM X-2713, 1974.

8. Goldberg, Theodore J.; and Hefner, Jerry N. (With appendix by James C. Emery): Starting Phenomena for Hypersonic Inlets With Thick Turbulent Boundary Layers at Mach 6. NASA TN D-6280, 1971.

9. Jones, Robert A.; and Hunt, James L.: Use of Fusible Temperature Indicators for Obtaining Quantitative Aerodynamic Heat-Transfer Data. NASA TR R-230, 1966.

10. Mockapertris, L. J.; and Chadwick, G. A.: Three-Dimensional Hypersonic Flow Boundary Layer Transition Distribution on Sharp 8-Degree Cone With Ablating and Non-Ablating Walls at Small Angles of Attack. BSD TR-67-197, U.S. Air Force, July 1967. (Available from DDC as AD 819 957.)

11. Kendall, J. M.: Wind Tunnel Experiments Relating to Supersonic and Hypersonic Boundary Layer Transition. AIAA Paper No. 74-133, Jan.-Feb. 1974.

12. Moeckel, W. E.: Some Effects of Bluntness on Boundary-Layer Transition and Heat Transfer at Supersonic Speeds. NACA Rep. 1312, 1957. (Supersedes NACA TN 3653.)

13. Stainback, P. Calvin (With appendix by P. Calvin Stainback and Kathleen C. Wicker): Effect of Unit Reynolds Number, Nose Bluntness, Angle of Attack, and Roughness on Transition on a 5° Half-Angle Cone at Mach 8. NASA TN D-4961, 1969.

14. Henderson, Arthur, Jr.: Hypersonic Viscous Flows. Modern Developments in Gas Dynamics, W. H. T. Loh, ed., Plenum Press, 1969, pp. 83-129.

15. Lomax, Harvard; and Inouye, Mamoru: Numerical Analysis of Flow Properties About Blunt Bodies Moving at Supersonic Speeds in an Equilibrium Gas. NASA TR R-204, 1964.

16. Inouye, Mamoru; and Lomax, Harvard: Comparison of Experimental and Numerical Results for the Flow of a Perfect Gas About Blunt-Nosed Bodies. NASA TN D-1426, 1962.

17. Price, Joseph M.; and Harris, Julius E.: Computer Program for Solving Compressible Nonsimilar-Boundary-Layer Equations for Laminar, Transitional, or Turbulent Flows of a Perfect Gas. NASA TM X-2458, 1972.

18. Harris, Julius E.: Numerical Solution of the Equations for Compressible Laminar, Transitional and Turbulent Boundary Layers and Comparisons With Experimental Data. NASA TR R-368, 1971.

19. Sims, Joseph L.: Tables for Supersonic Flow Around Right Circular Cones at Small Angle of Attack. NASA SP-3004, 1964.

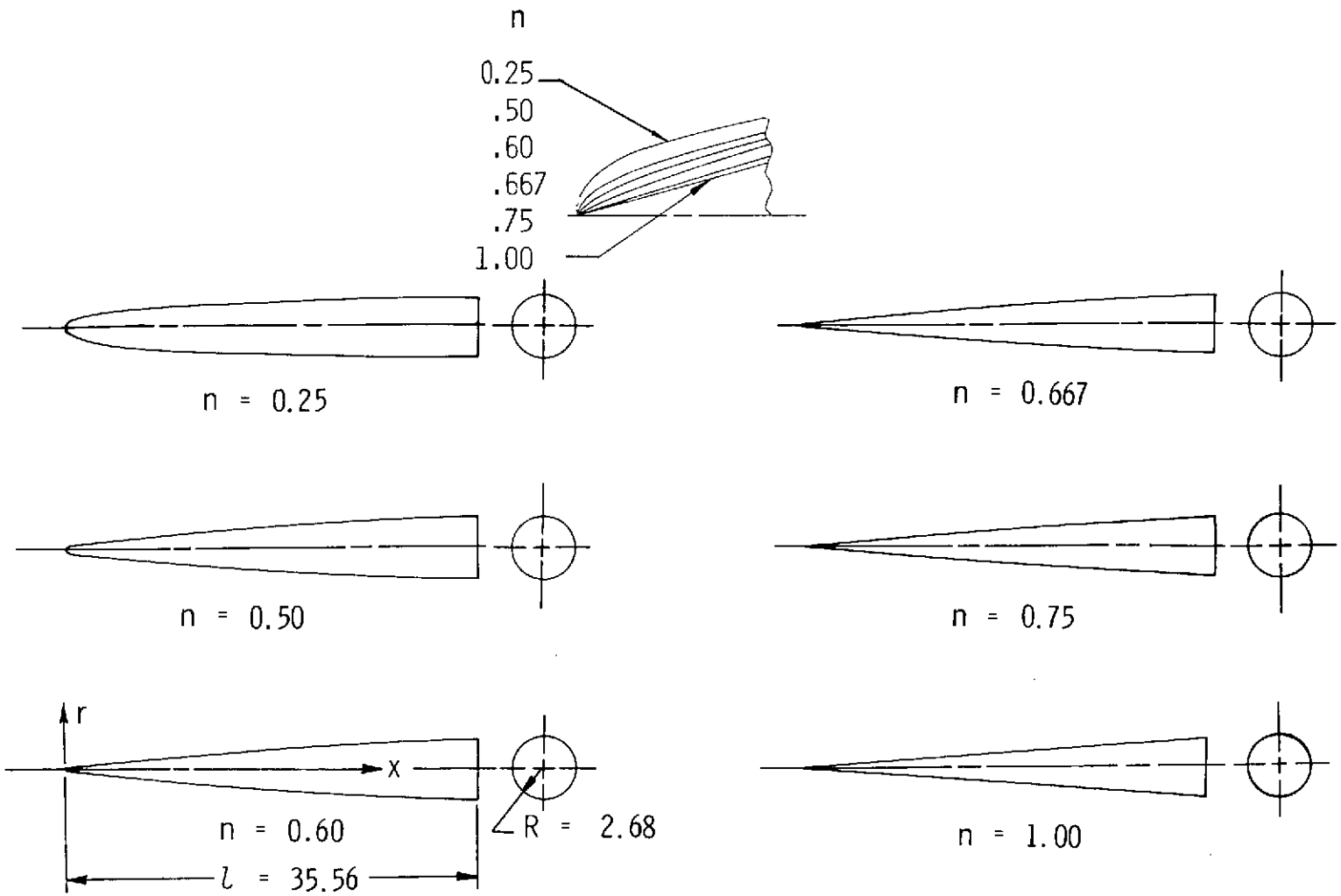

Figure 1.- Power-law bodies studied. (All dimensions are in cm.) Model shape equation: $\frac{r}{R} = \left(\frac{x}{l}\right)^n$.

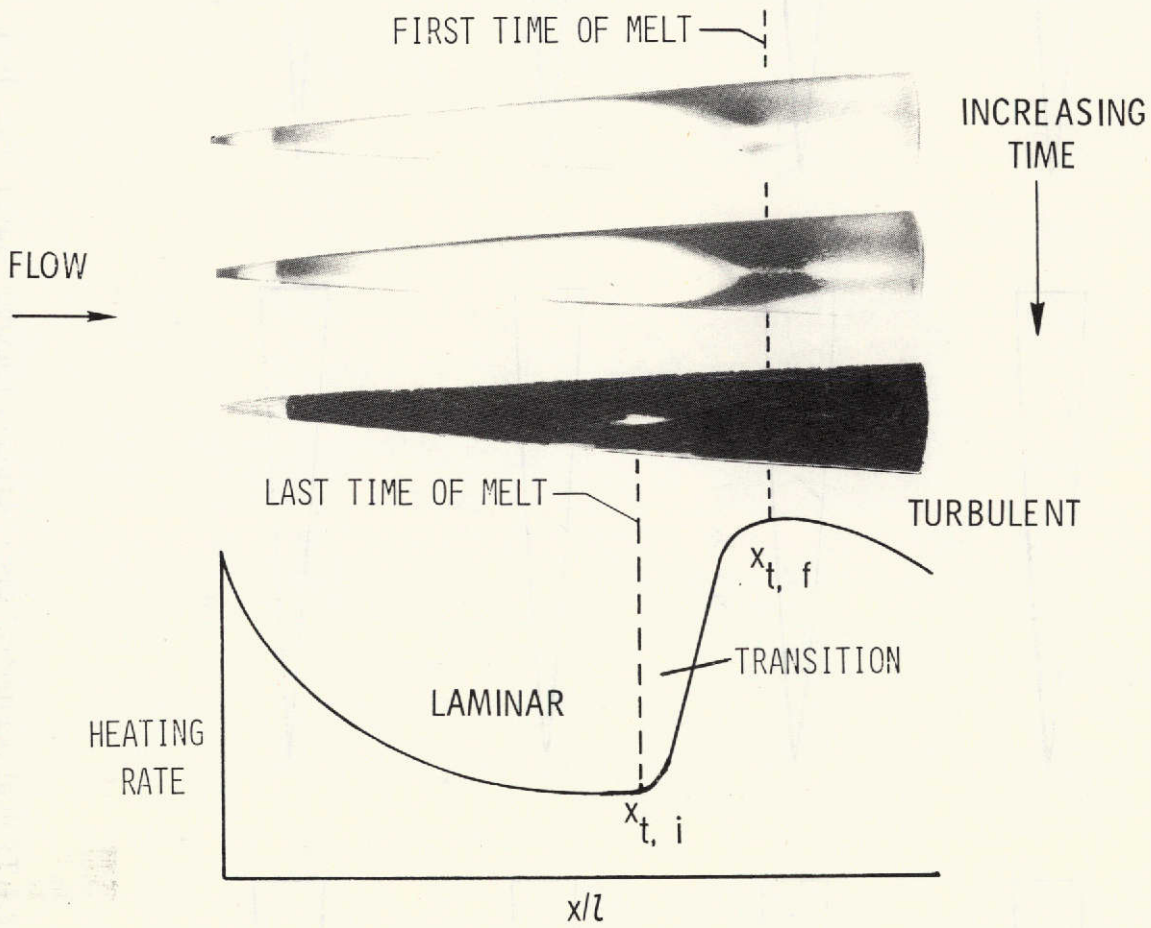

L-74-1137

Figure 2.- Typical time history of phase change relative to local conditions of boundary layer.

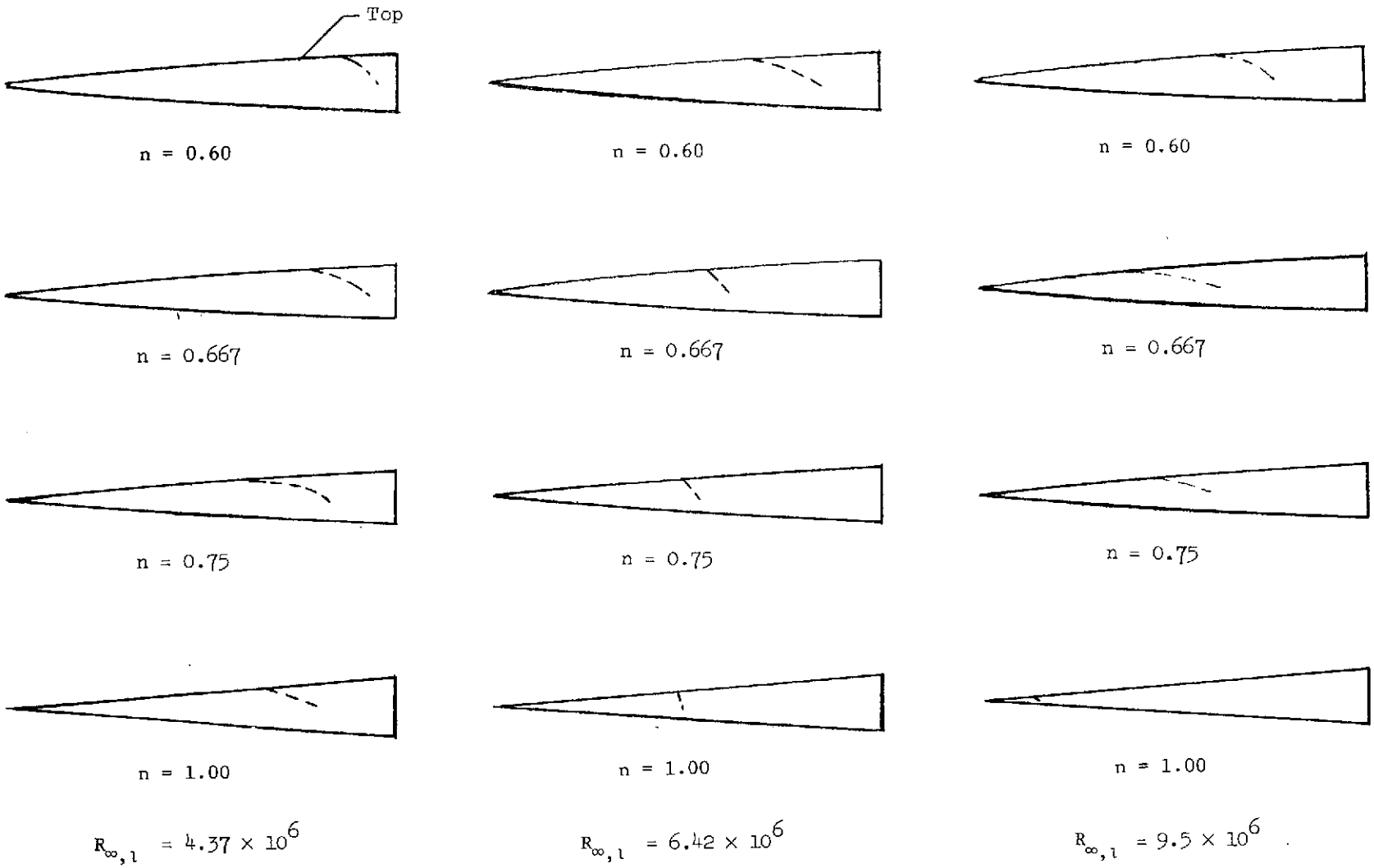

Figure 3.- Typical peripheral distribution of boundary-layer transition.

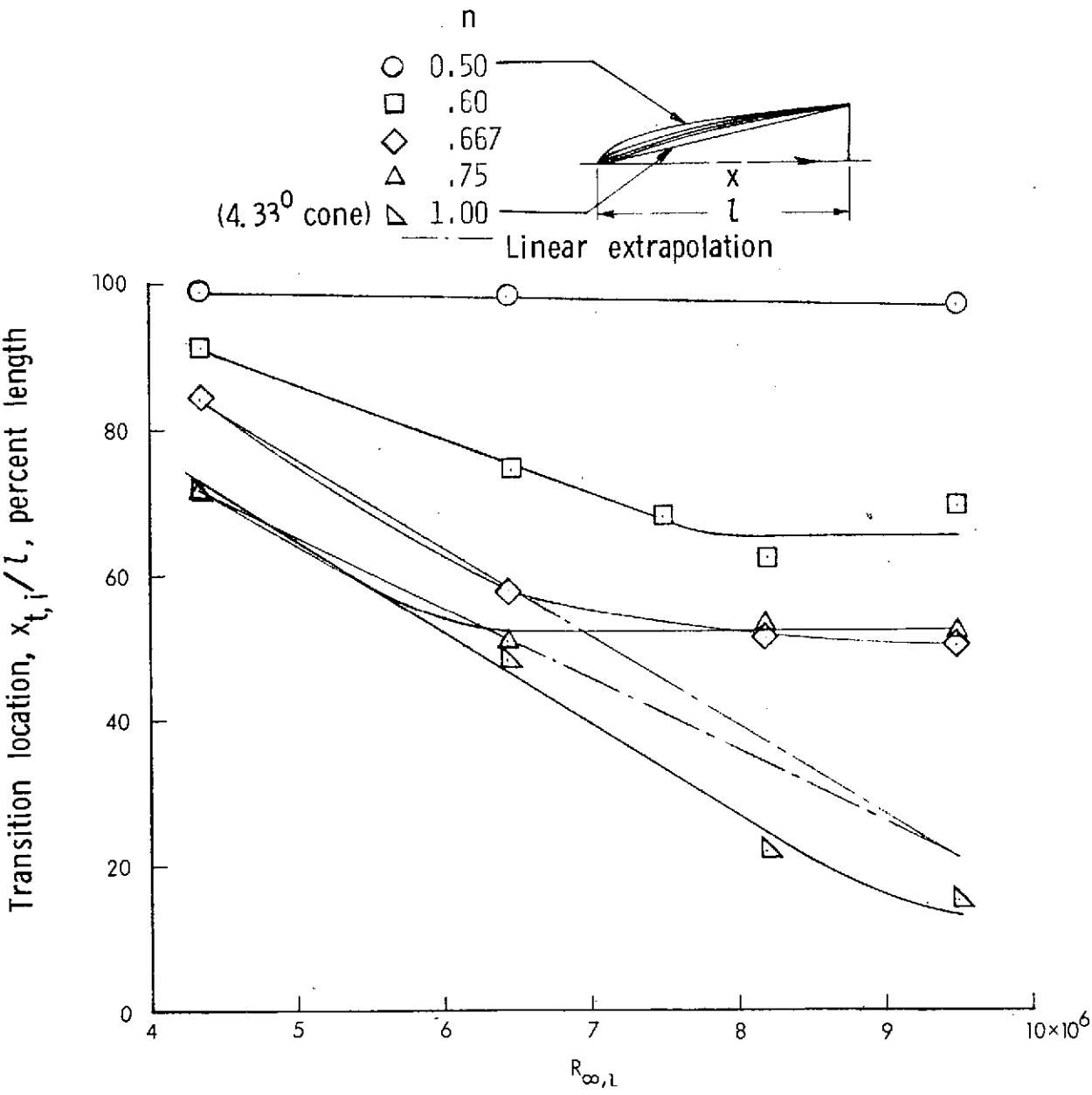

Figure 4.- Average measured location of initial boundary-layer transition on n-powered bodies at Mach number of 6 using phase-change coatings.

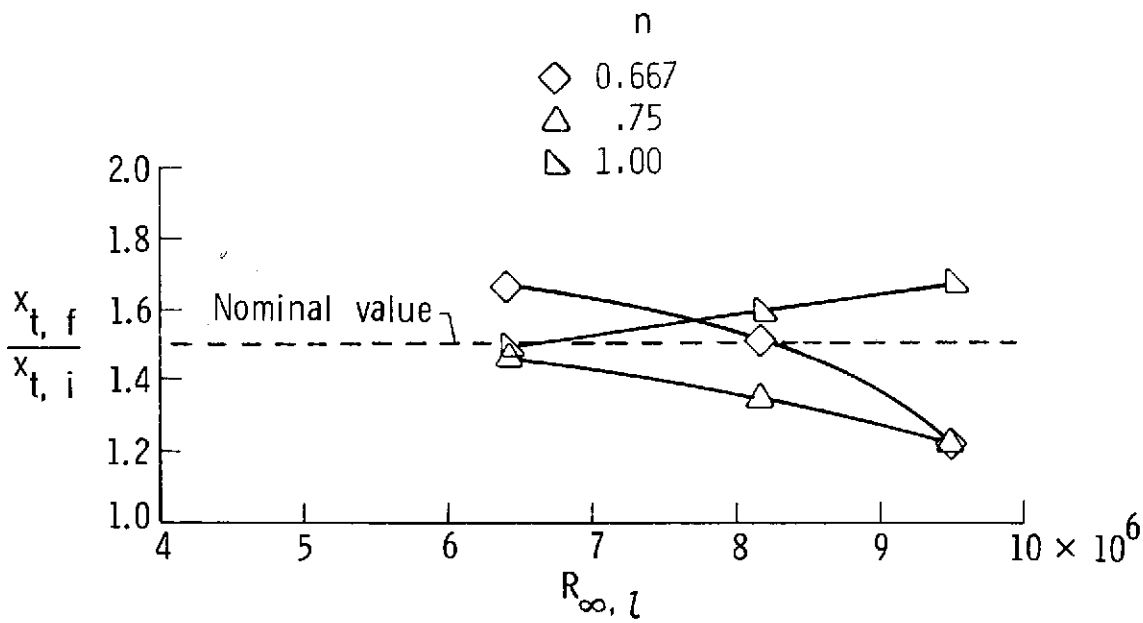

Figure 5.- Ratio of average measured location of end of transition to initiation of transition on n-powered bodies at Mach number of 6.

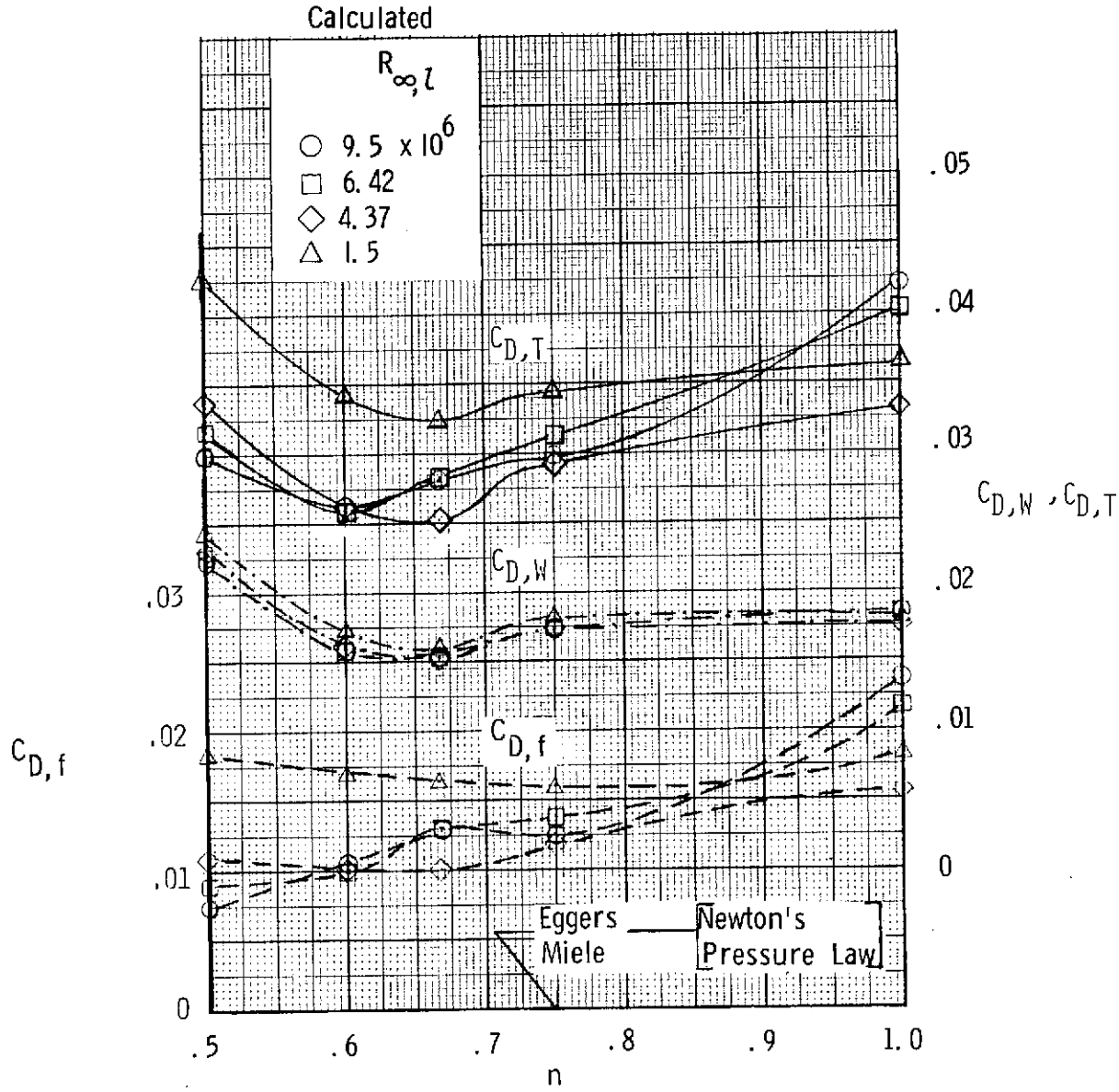

Figure 6.- Variation of calculated skin-friction, wave, and total-drag coefficients with power-law exponent in model shape equation $\frac{r}{R} = \left(\frac{x}{l}\right)^n$. Measured transition locations and boundary-layer displacement-thickness effects are included.

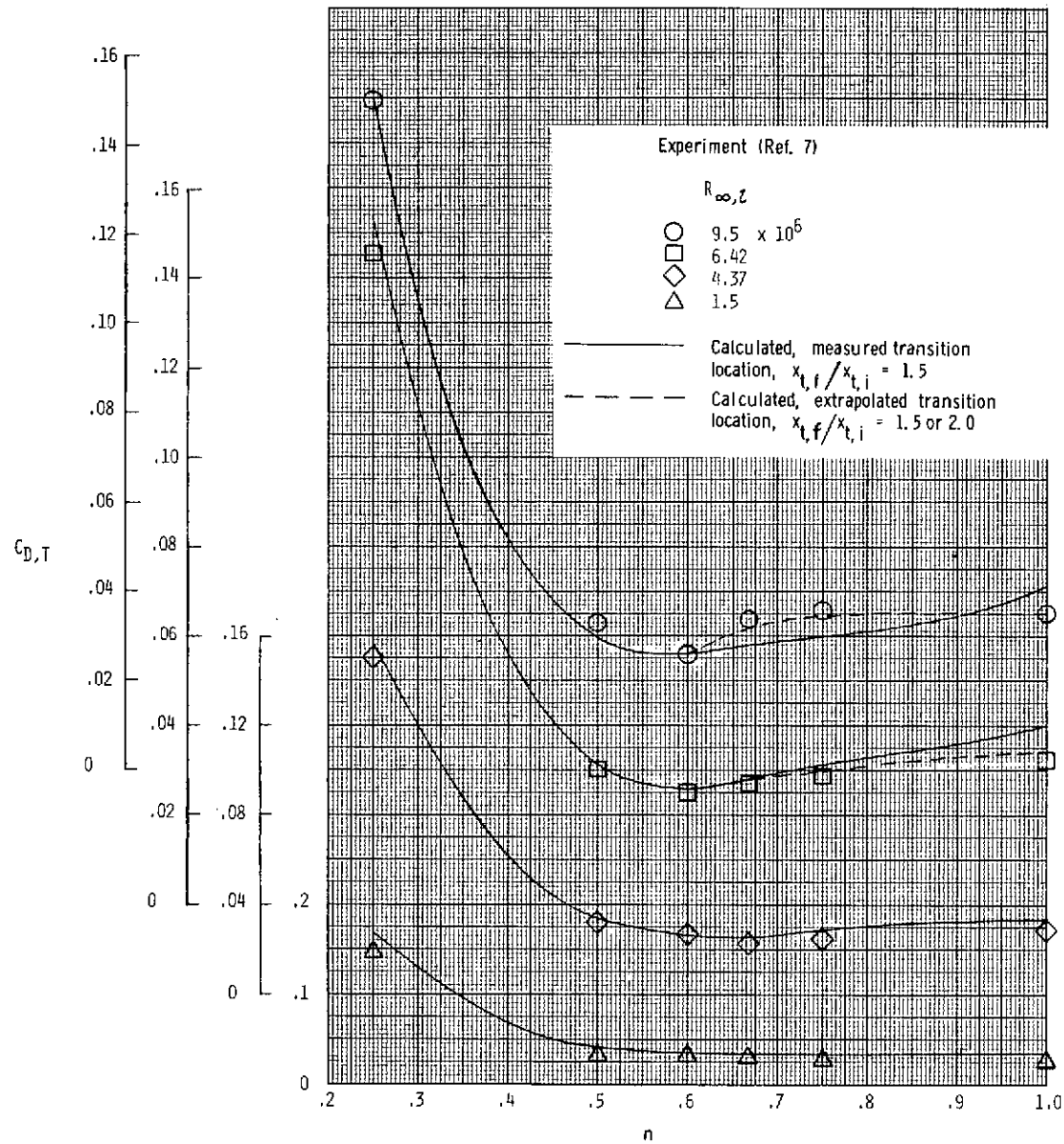

Figure 7.- Comparison of experimental and calculated total-drag coefficients for six power-law bodies at Mach number of 6 and four Reynolds numbers.

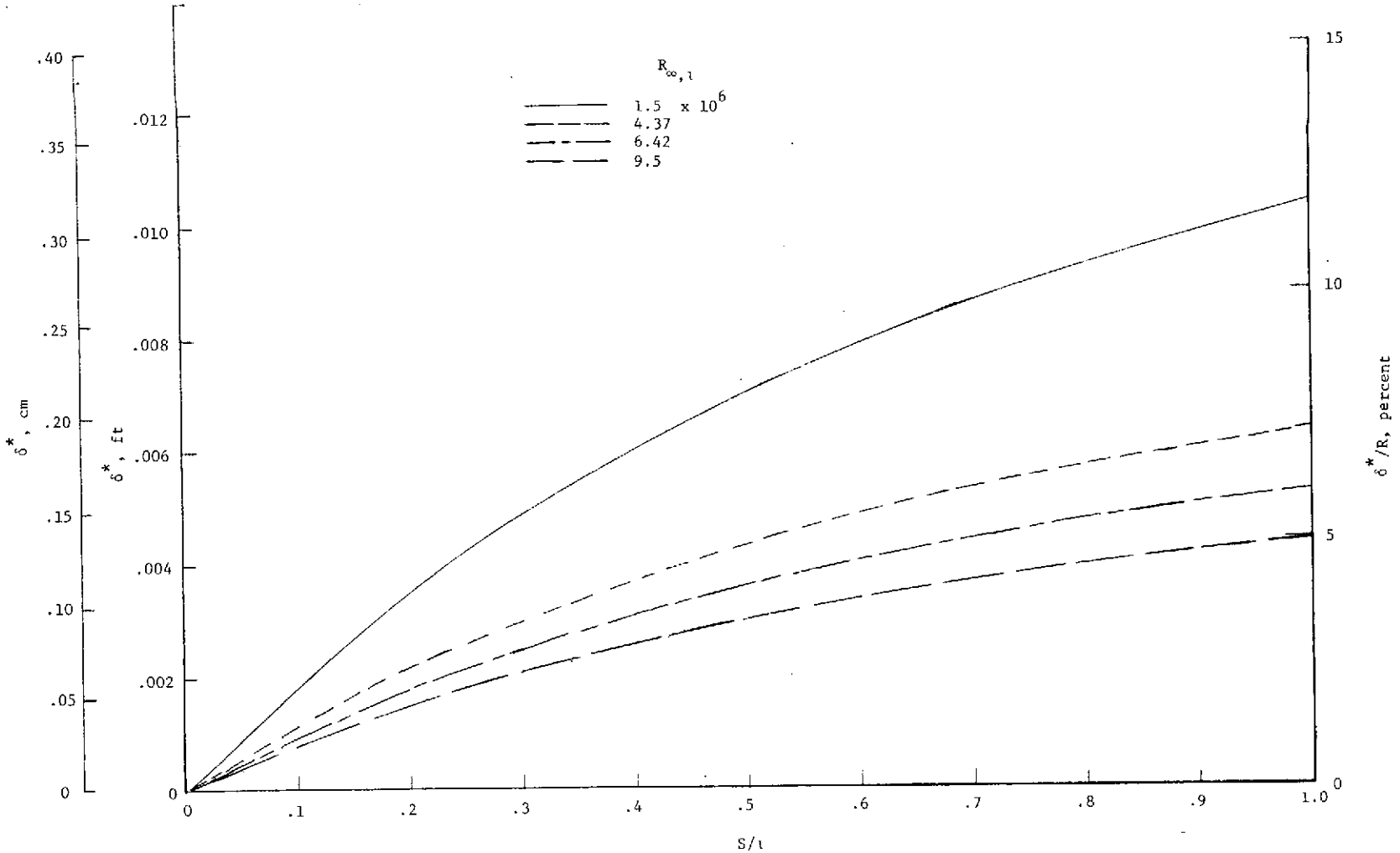

(a) n = 0.25.

Figure 8.- Variation of boundary-layer displacement thickness along body surface for four Reynolds numbers. Tick marks locate beginning of transition.

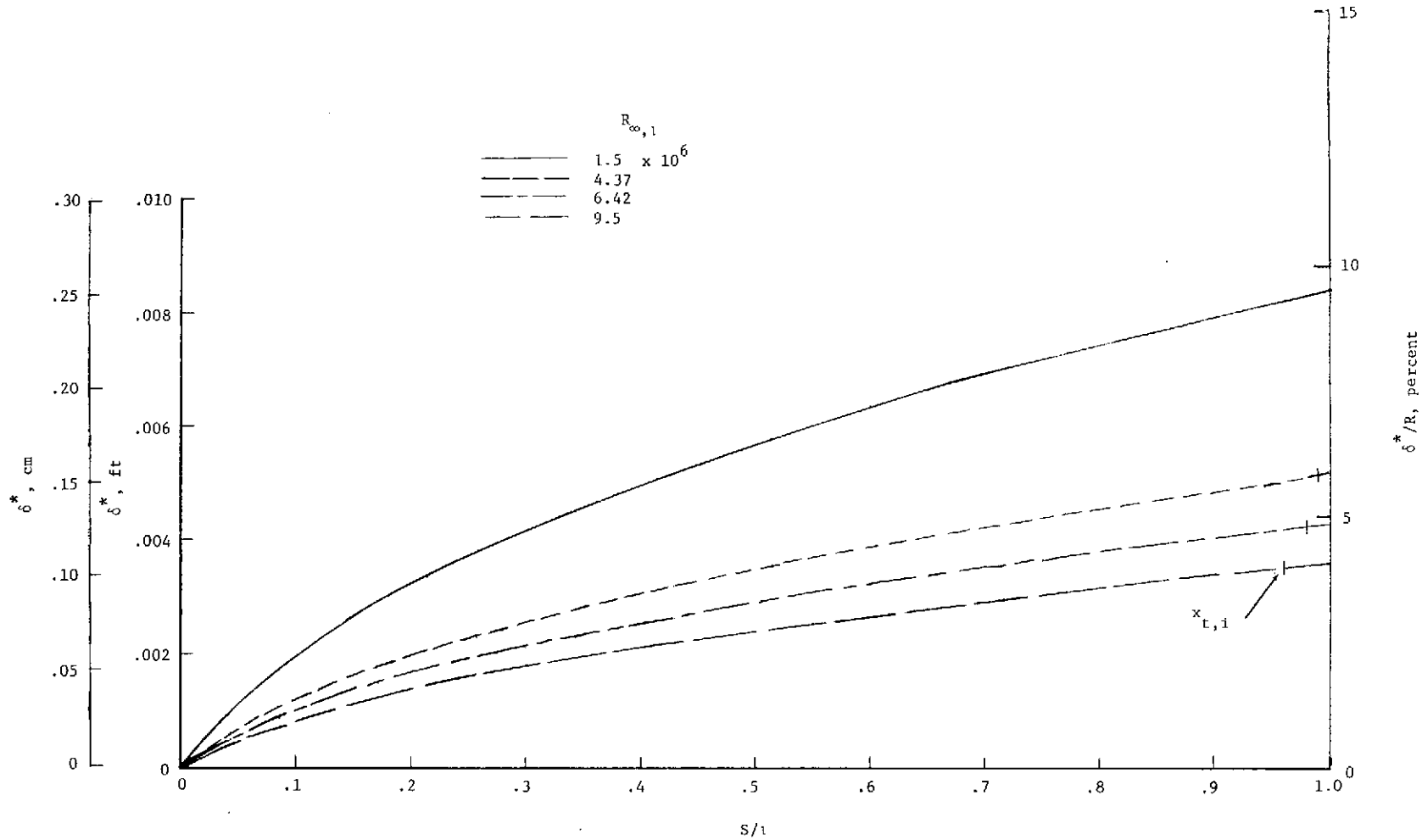

(b) n = 0.50.

Figure 8.- Continued.

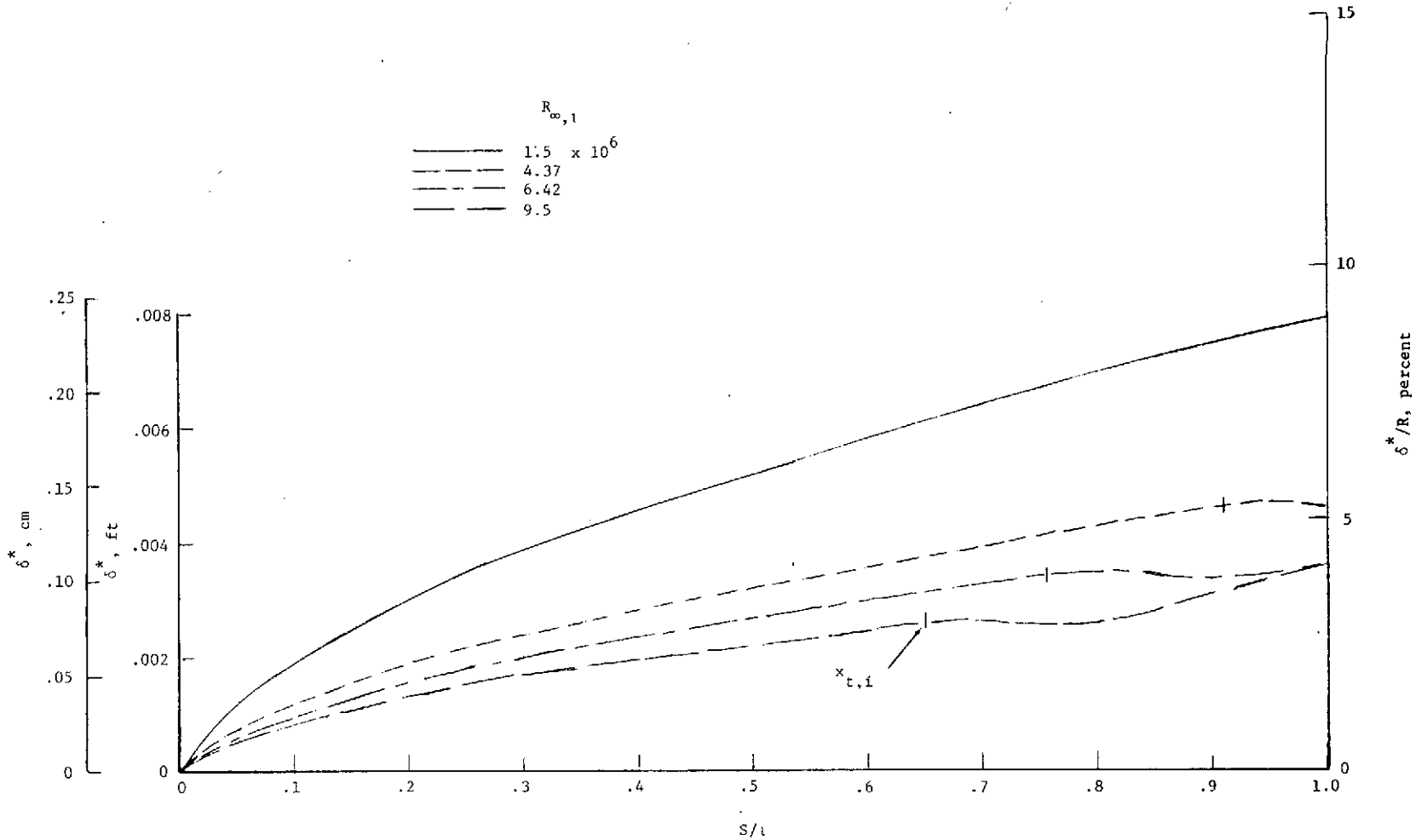

(c) n = 0.60.

Figure 8.- Continued.

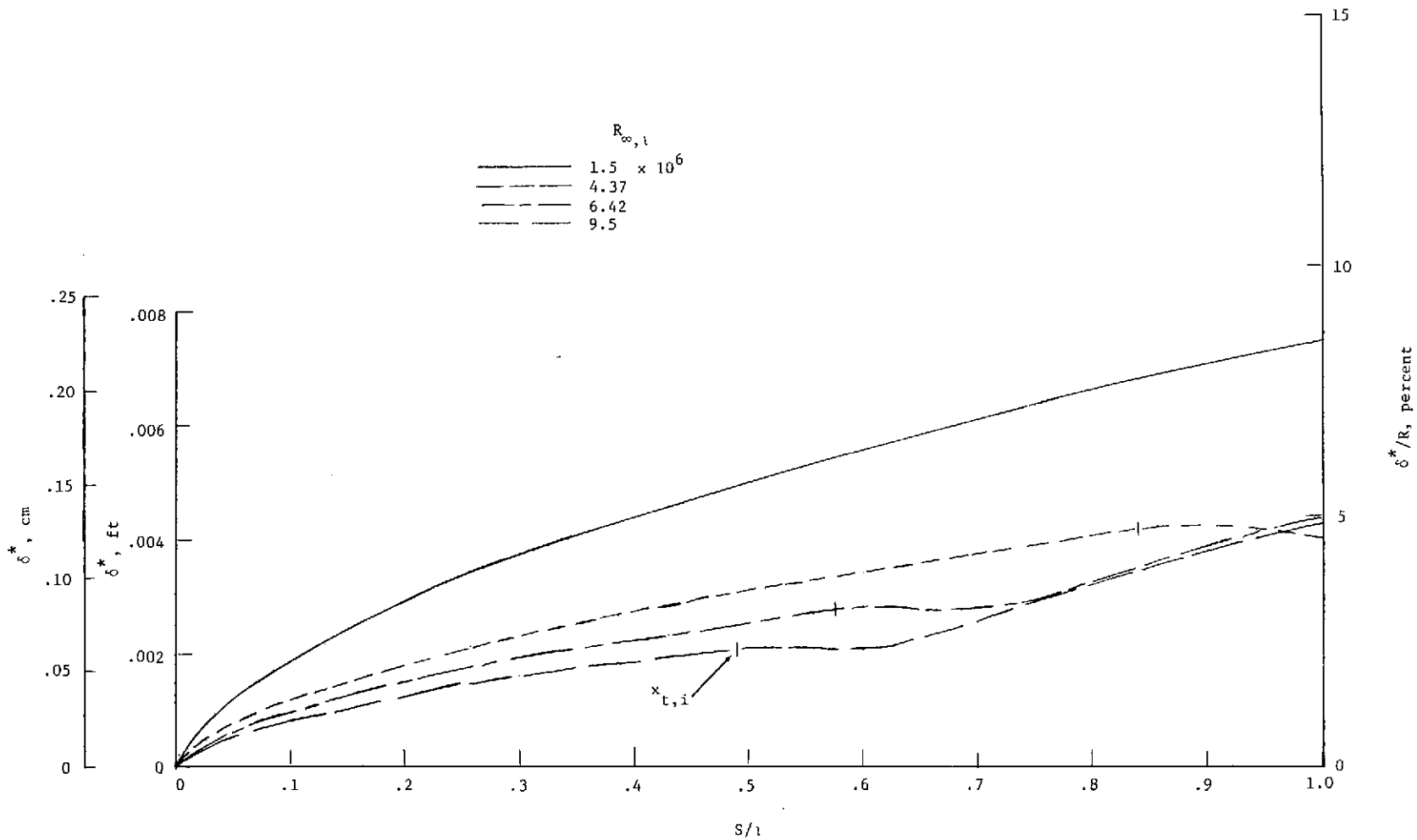

(d) n = 0.667.

Figure 8.- Continued.

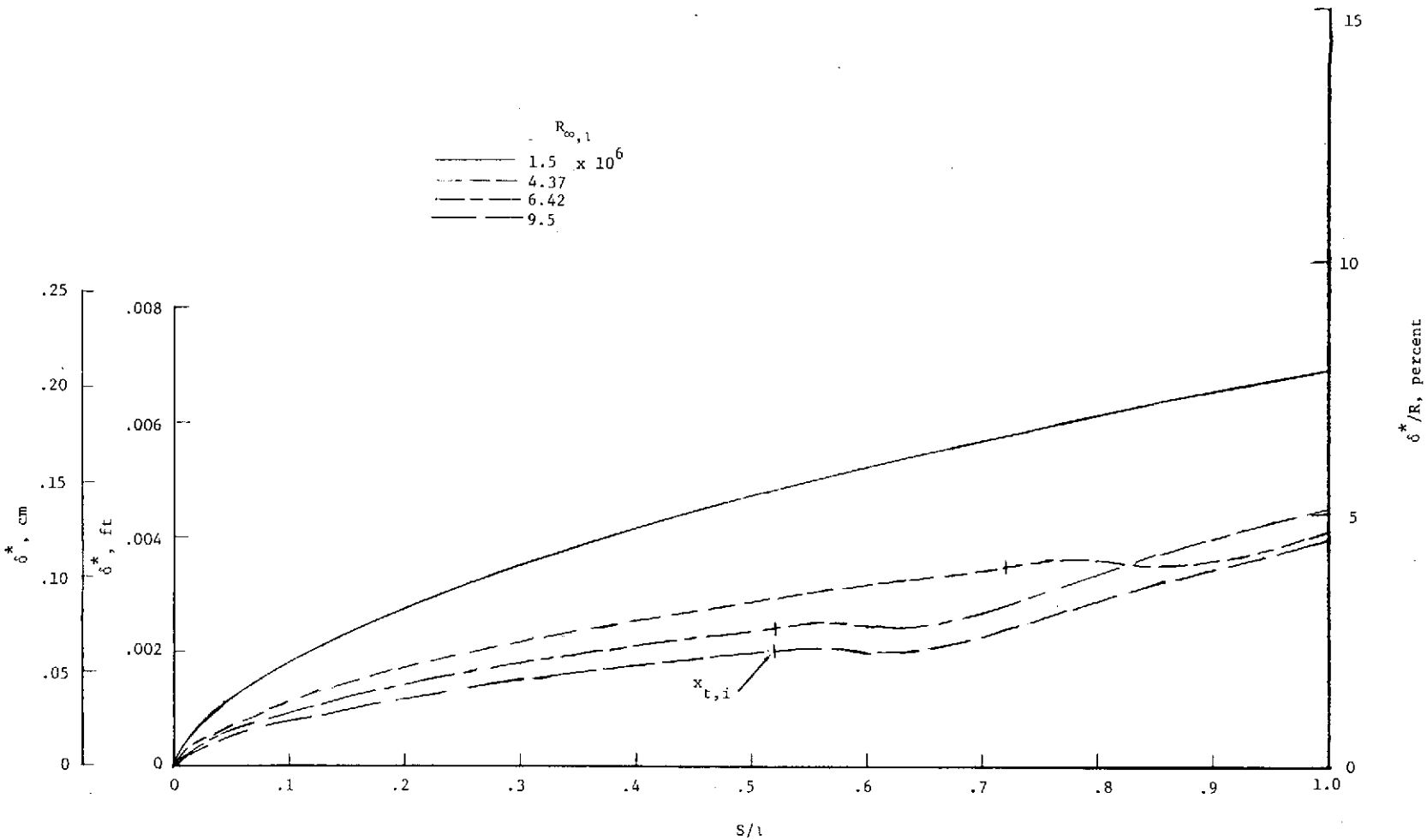

(e) n = 0.75.

Figure 8.- Continued.

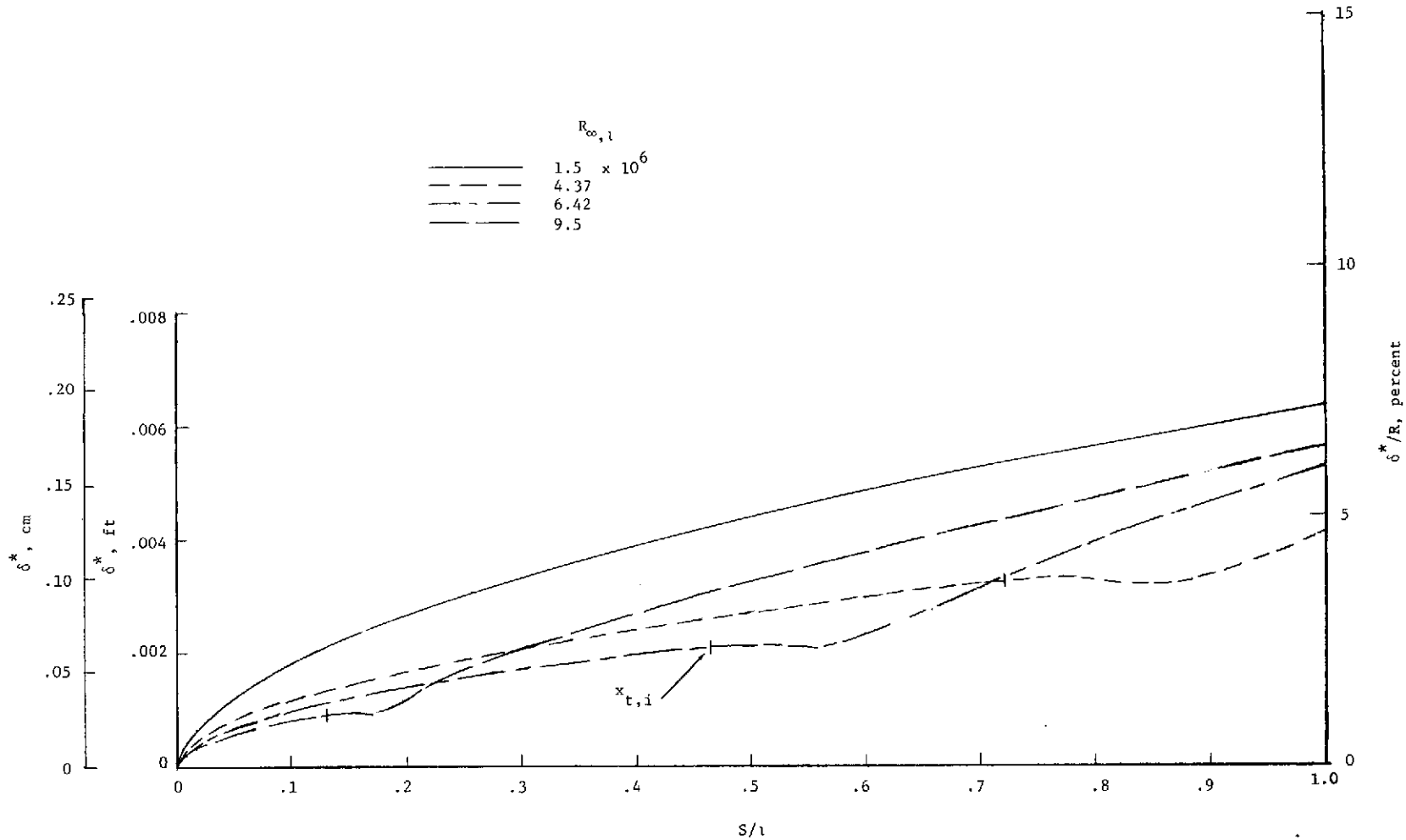

(f) n = 1.00.

Figure 8.- Concluded.

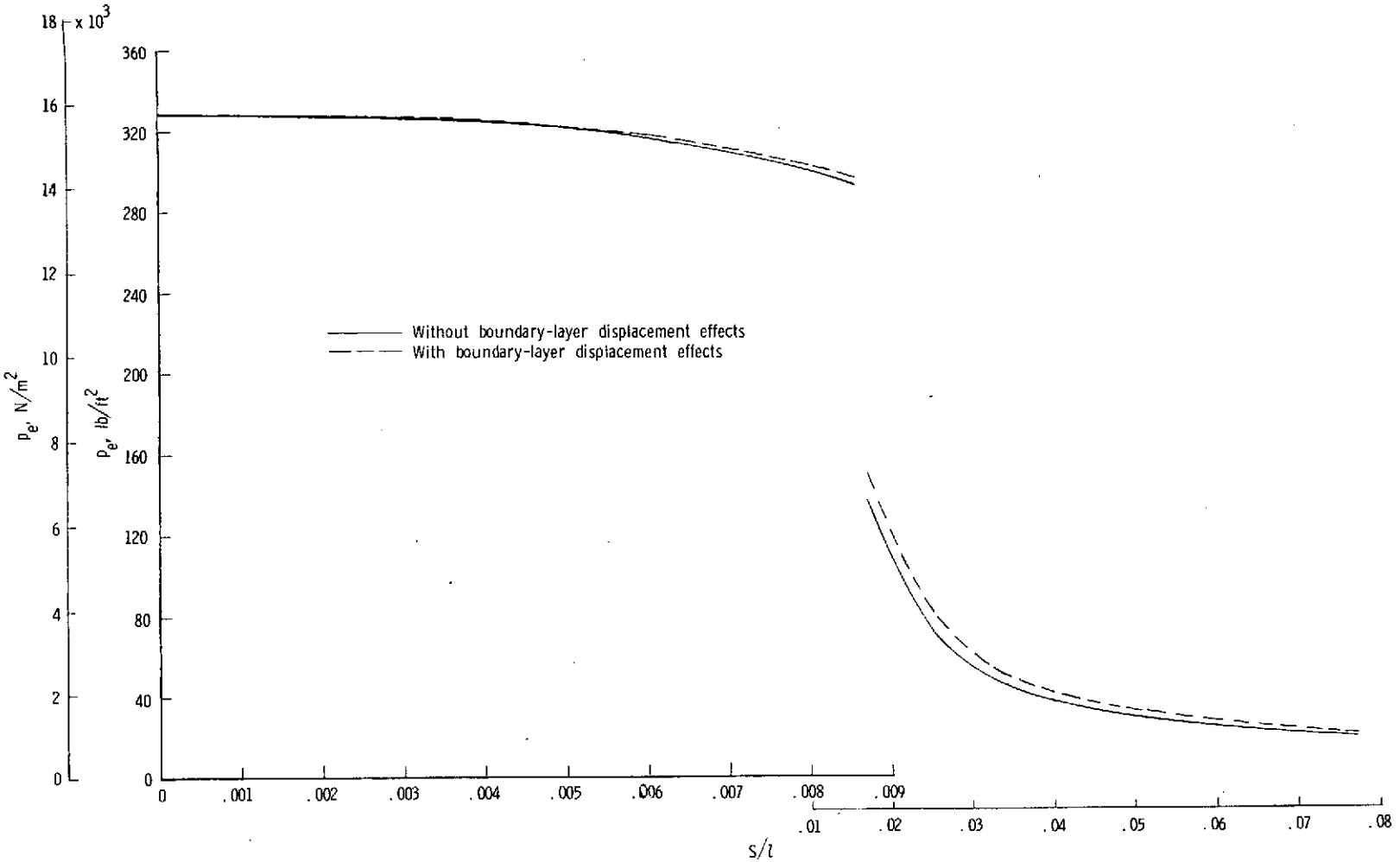

(a) $n = 0.25$; $R_{\infty,l} = 1.5 \times 10^6$.

Figure 9.- Effect of boundary-layer displacement thickness on pressure distribution of each body at minimum and maximum Reynolds numbers.

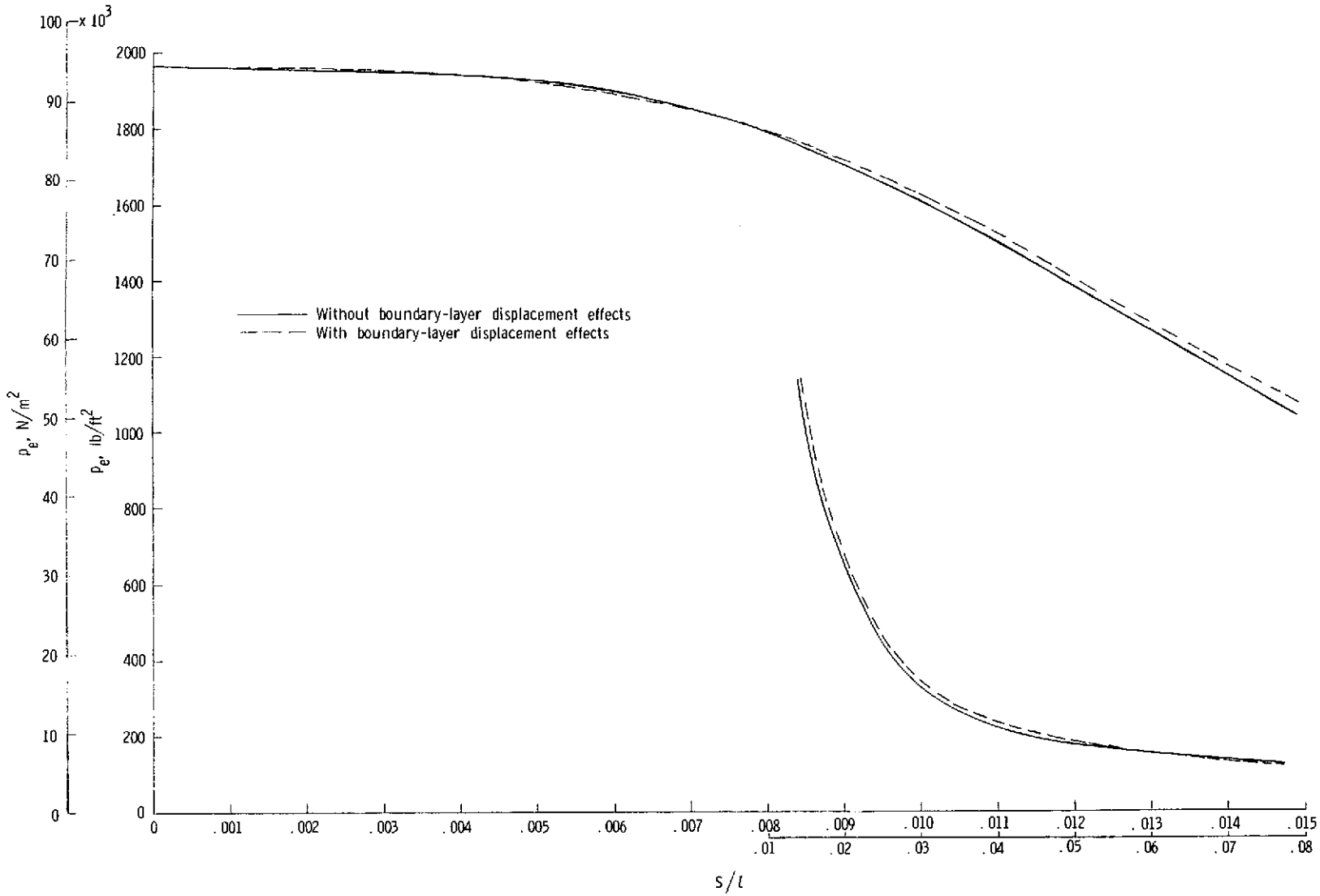

(b) n = 0.25; $R_{\infty,l} = 9.5 \times 10^6$.

Figure 9.- Continued.

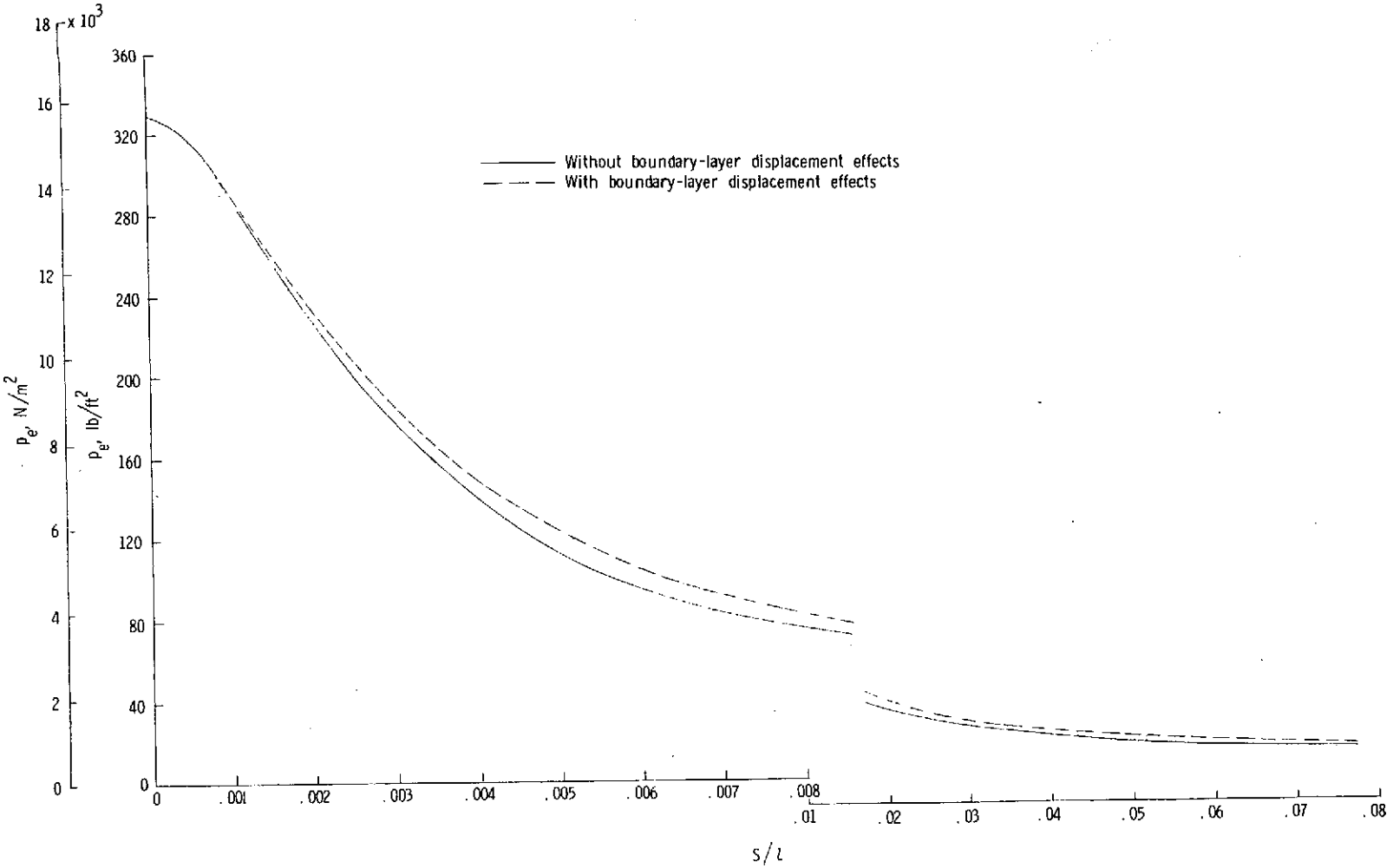

(c) n = 0.50; $R_{\infty,\ell} = 1.5 \times 10^6$.

Figure 9.- Continued.

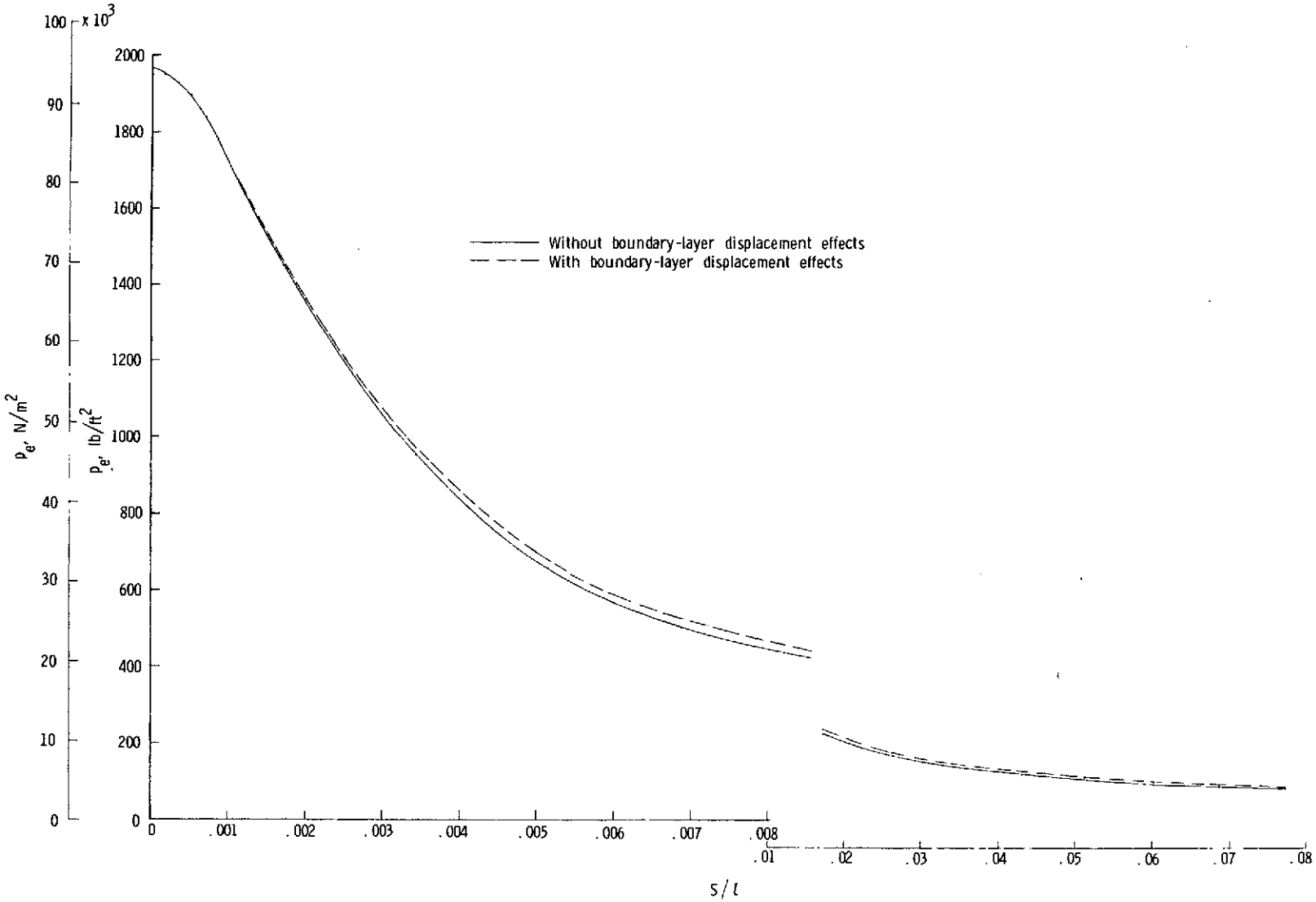

(d) n = 0.50; $R_{\infty,l} = 9.5 \times 10^6$.

Figure 9.- Continued.

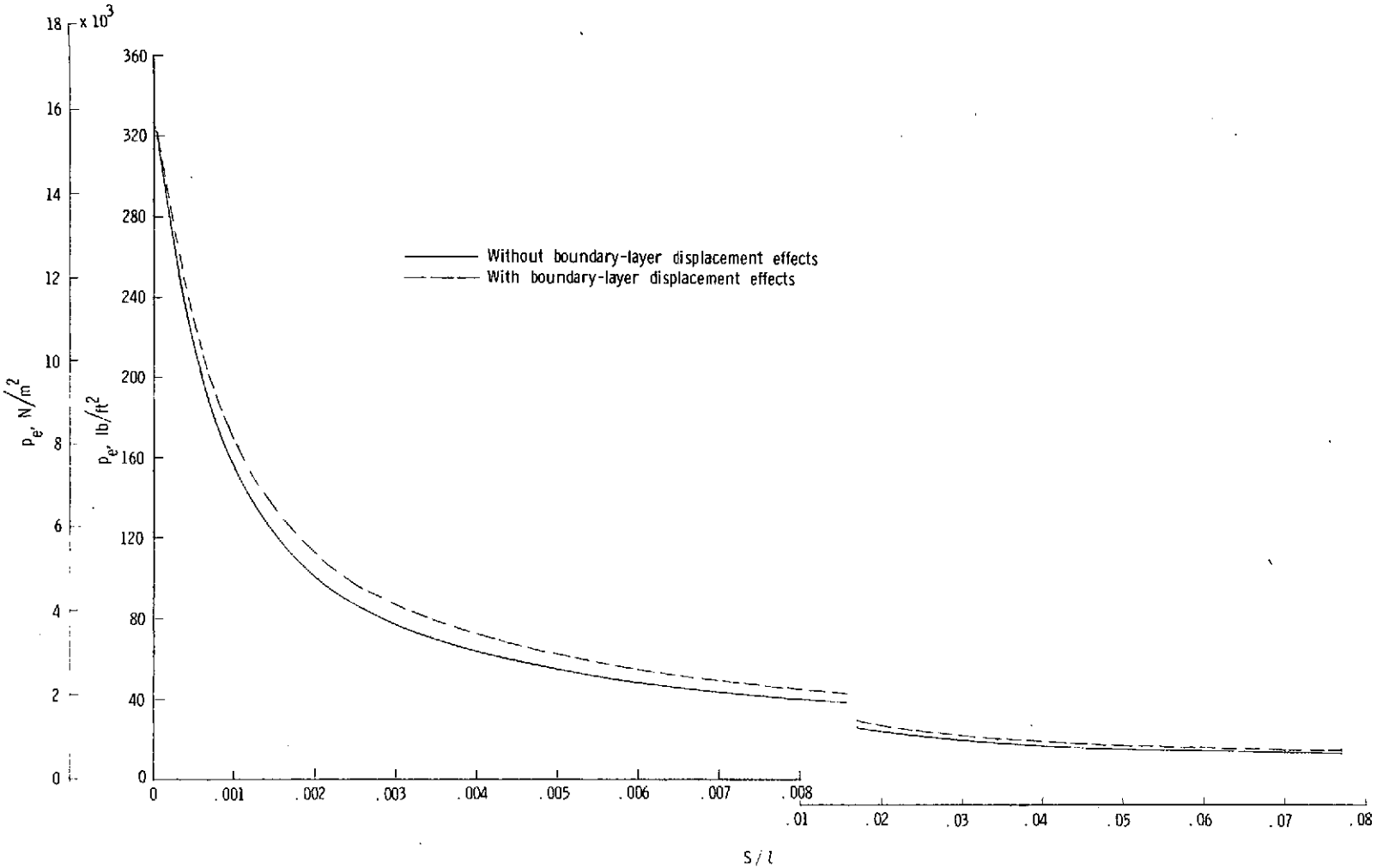

(e) n = 0.60; $R_{\infty,l} = 1.5 \times 10^6$.

Figure 9.- Continued.

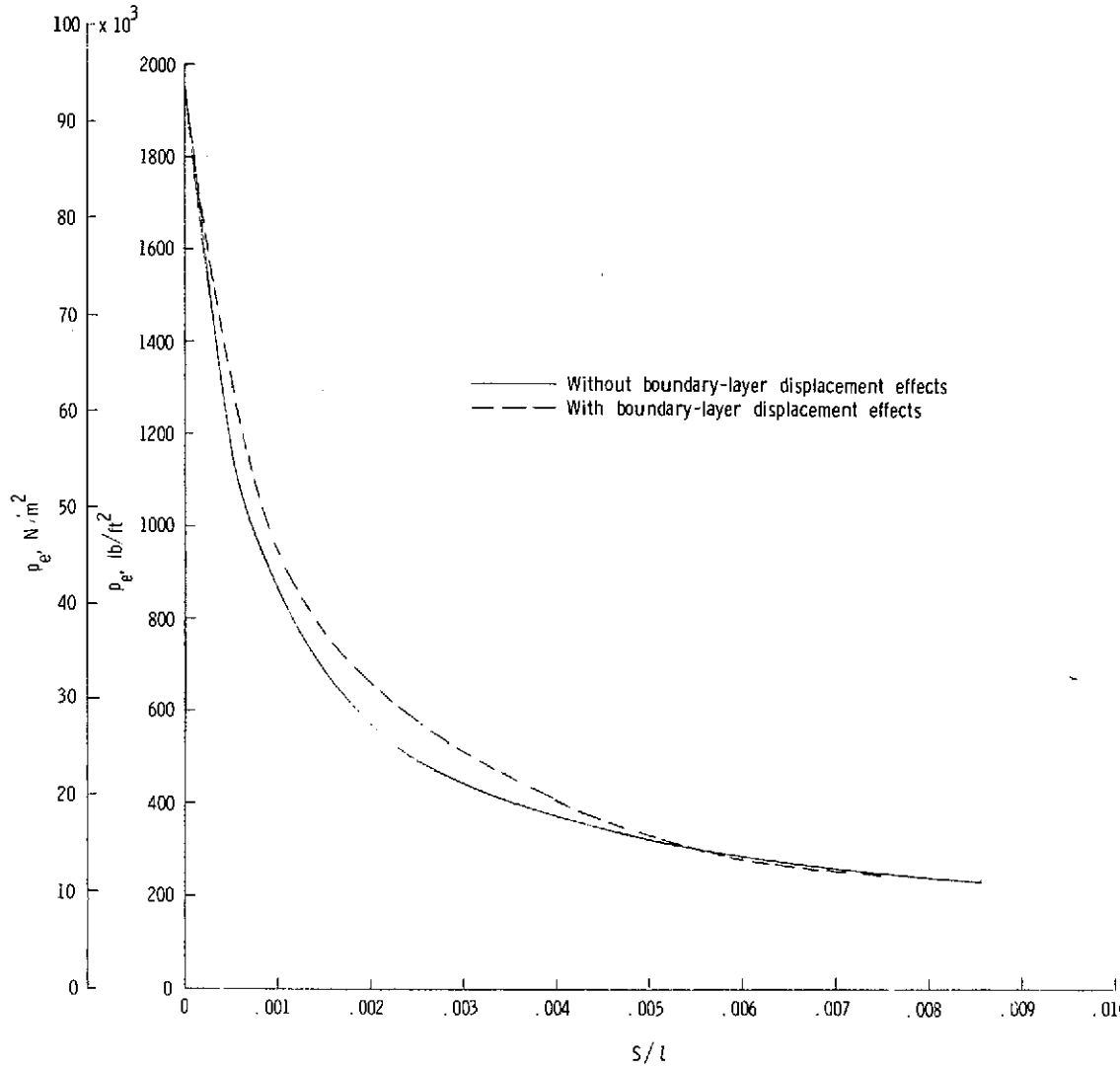

(f) n = 0.60; $R_{\infty,l} = 9.5 \times 10^6$.

Figure 9.- Continued.

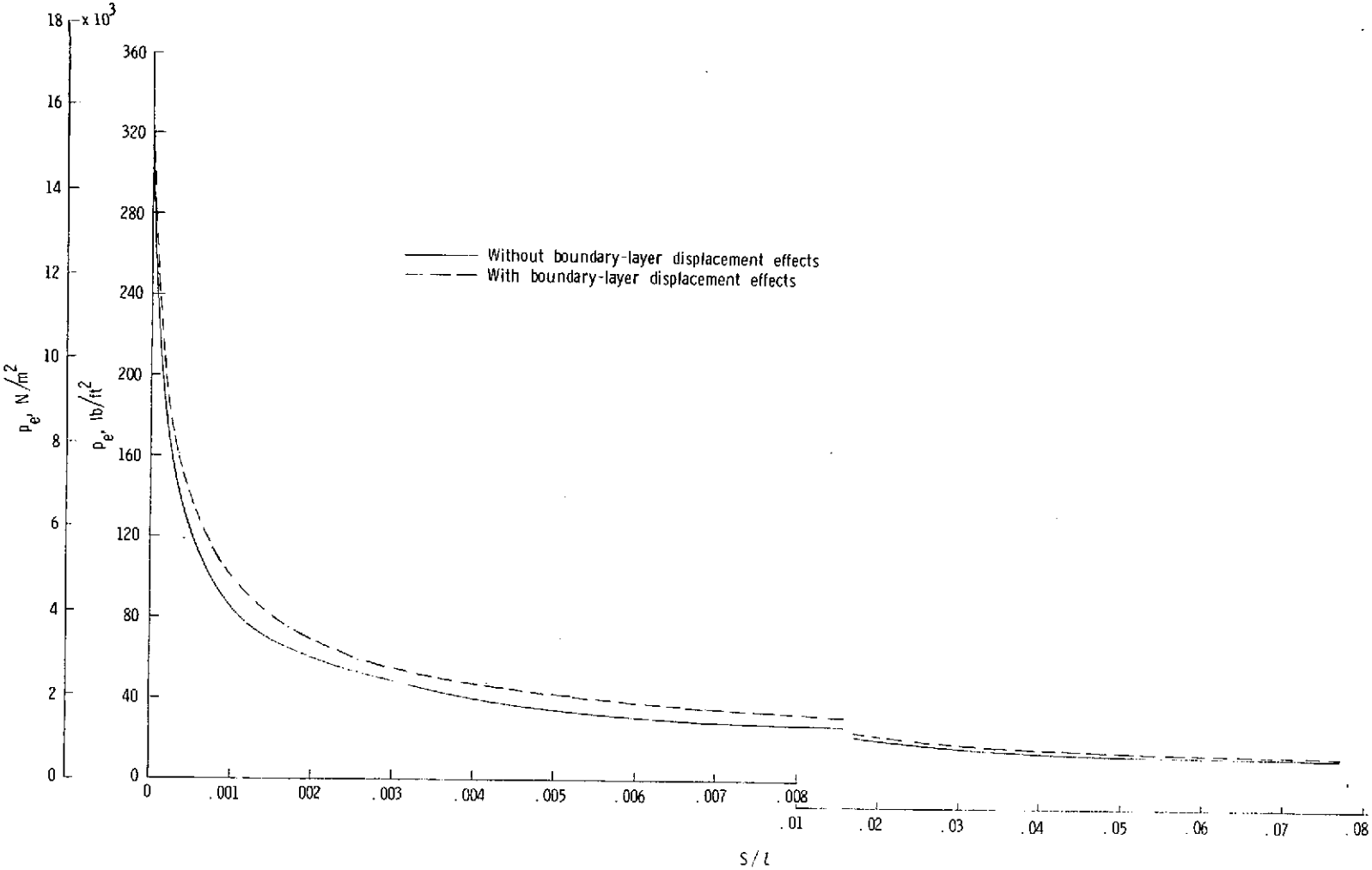

(g) n = 0.667; $R_{\infty,\ell} = 1.5 \times 10^6$.

Figure 9.- Continued.

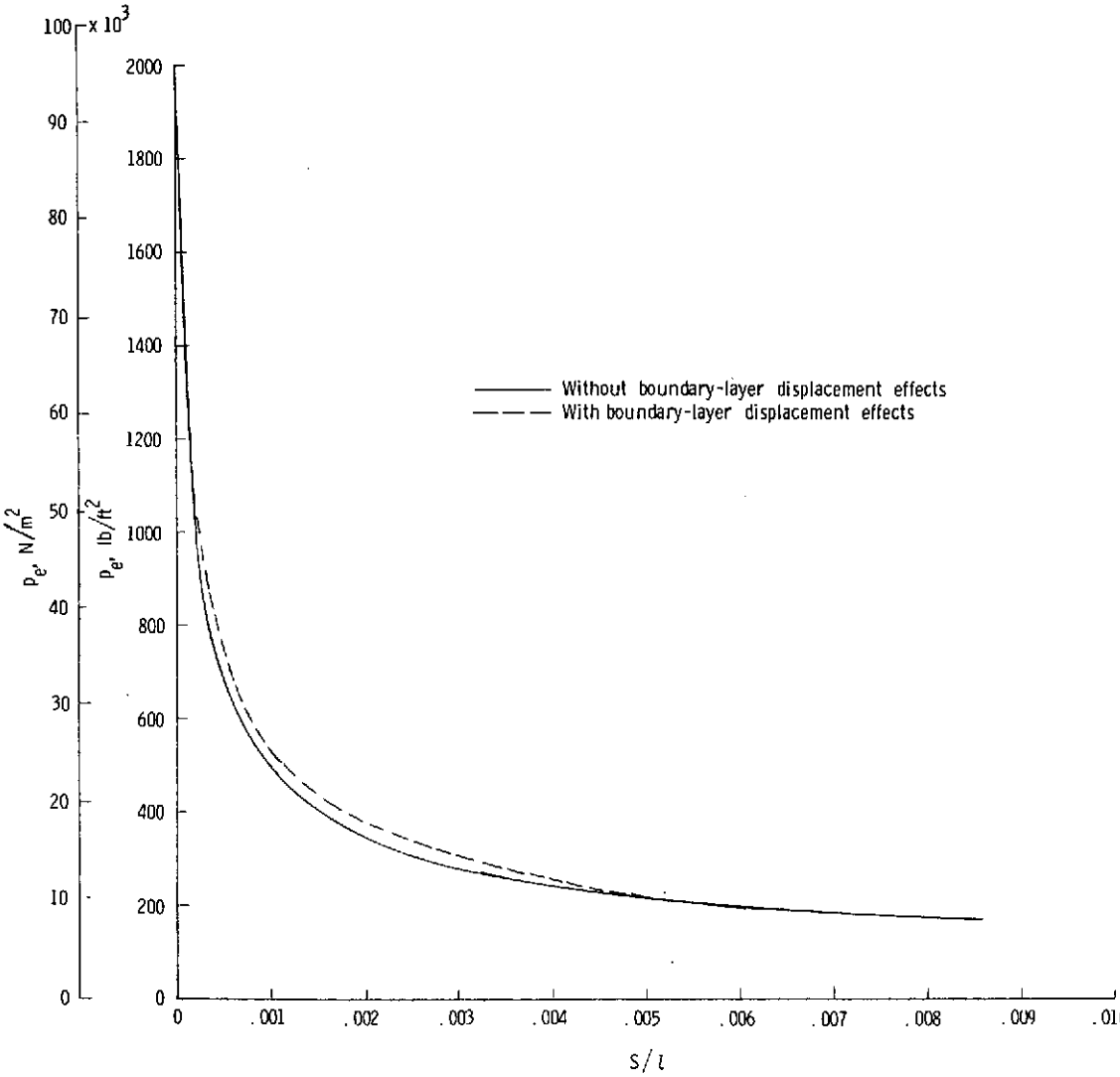

(h) n = 0.667; $R_{\infty,l} = 9.5 \times 10^6$.

Figure 9.- Continued.

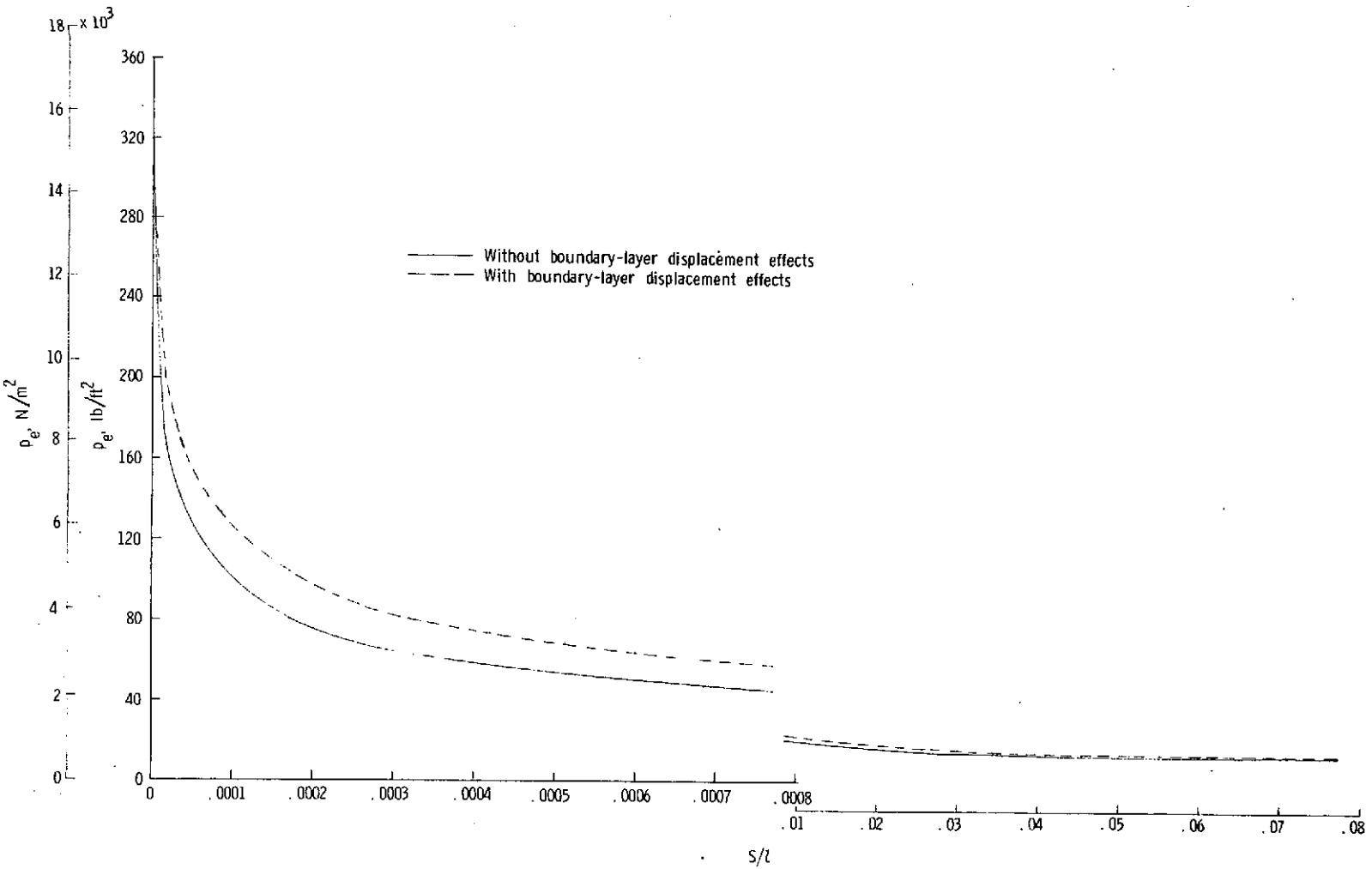

(i) $n = 0.75$; $R_{\infty,\ell} = 1.5 \times 10^6$.

Figure 9.- Continued.

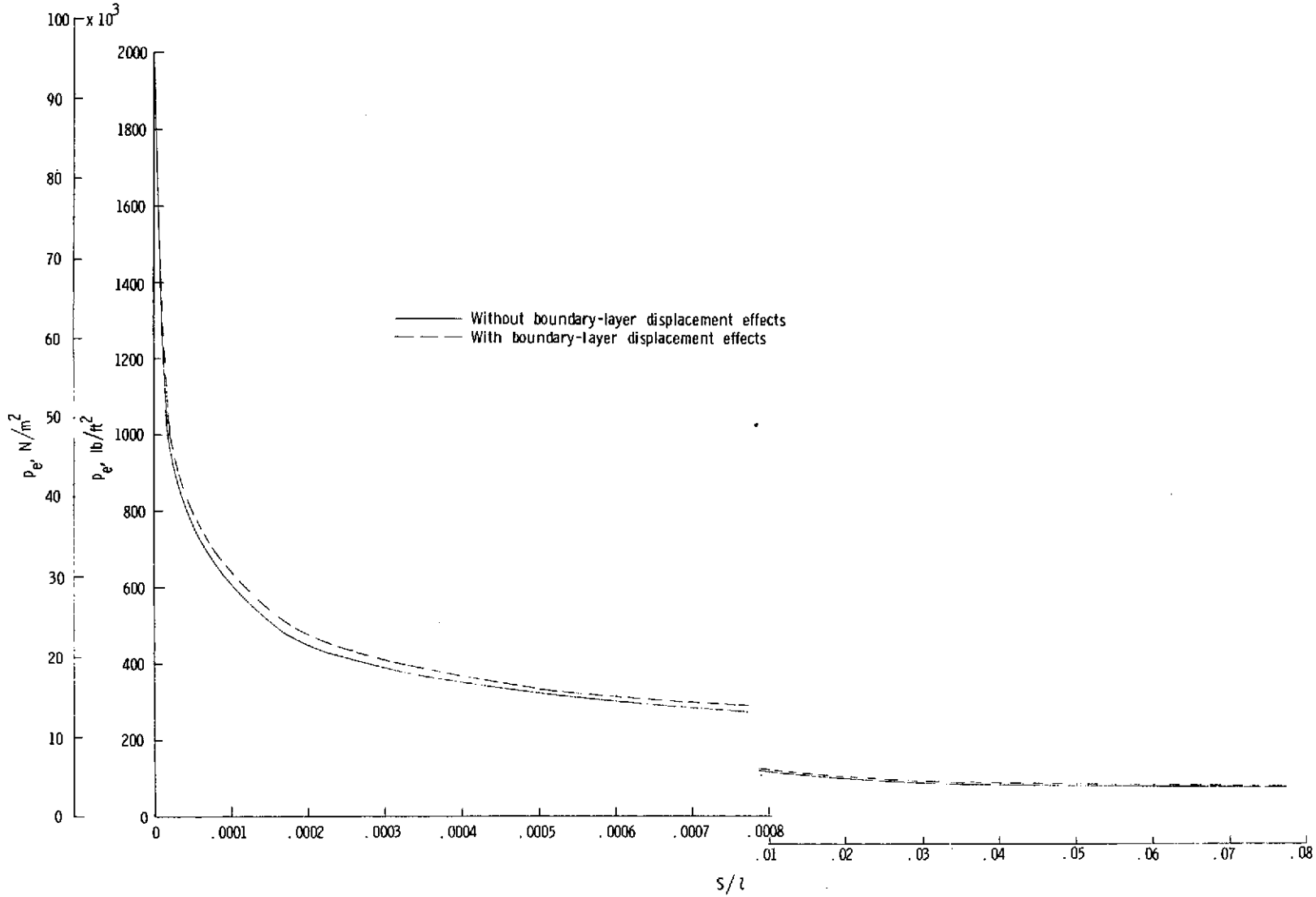

(j) n = 0.75; $R_{\infty,l} = 9.5 \times 10^6$.

Figure 9.- Continued.

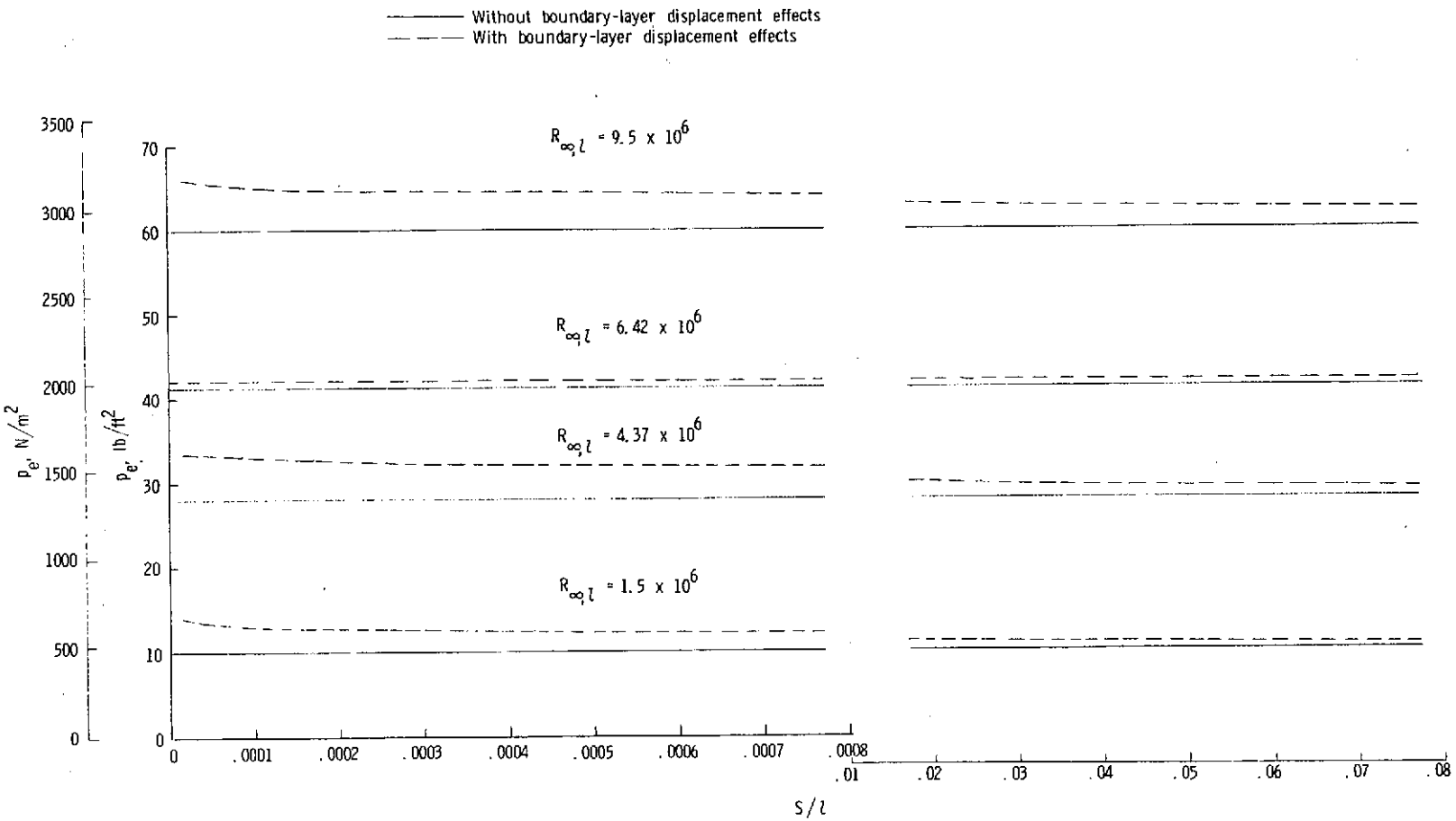

(k) n = 1.00.

Figure 9.- Concluded.

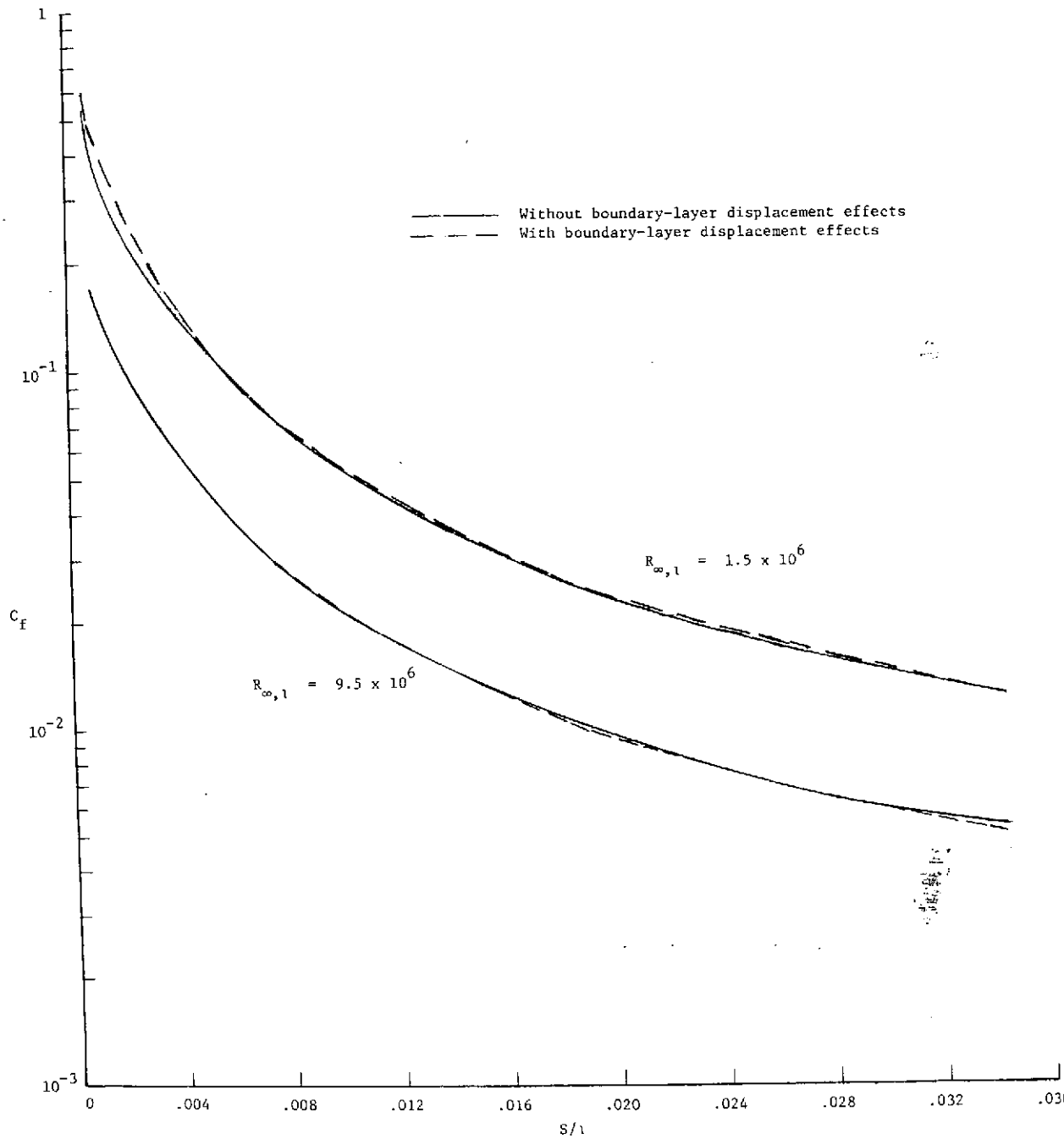

(a) n = 0.25.

Figure 10.- Effect of boundary-layer displacement thickness on skin-friction distribution of each body at minimum and maximum Reynolds numbers.

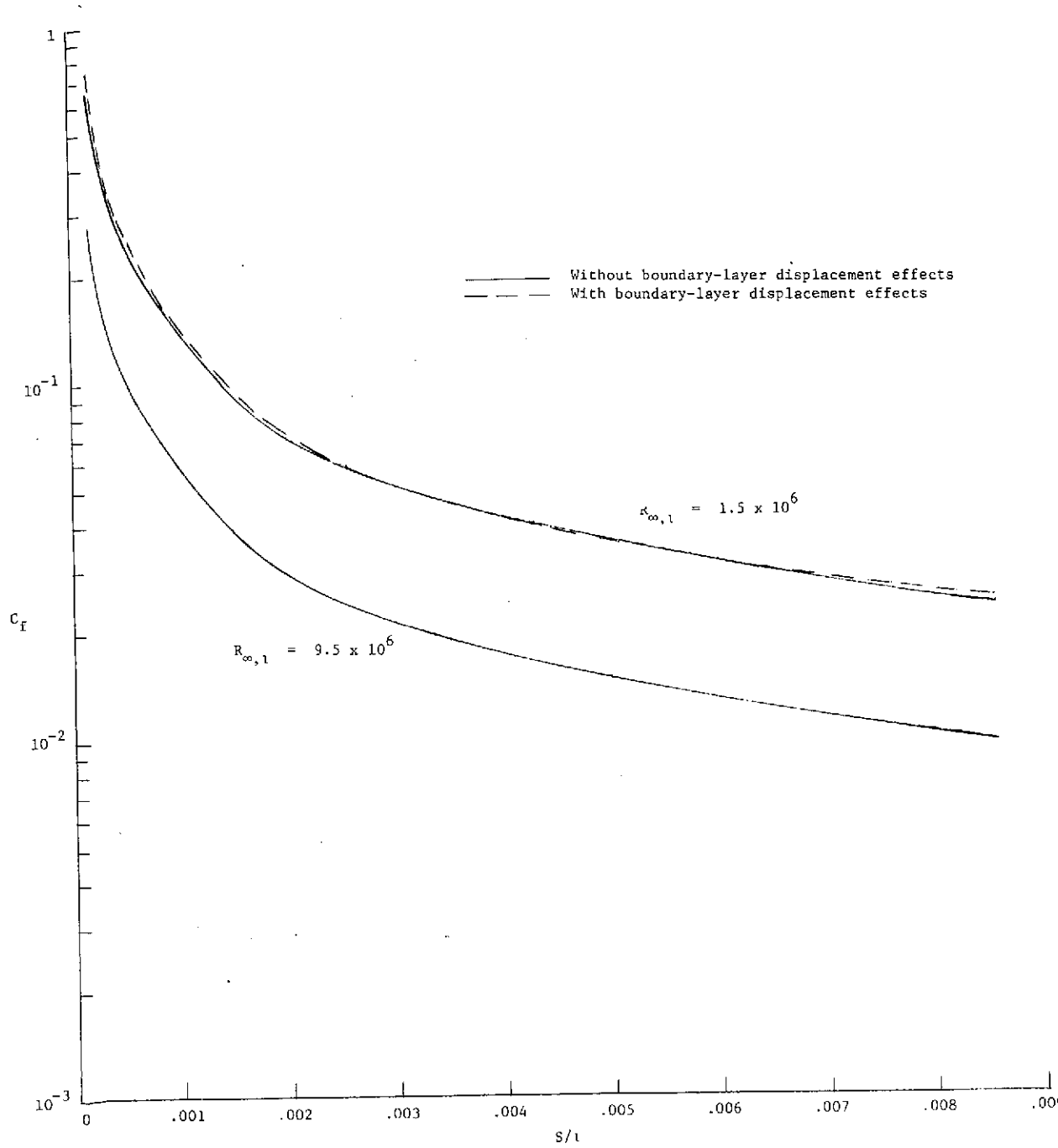

(b) n = 0.50.

Figure 10.- Continued.

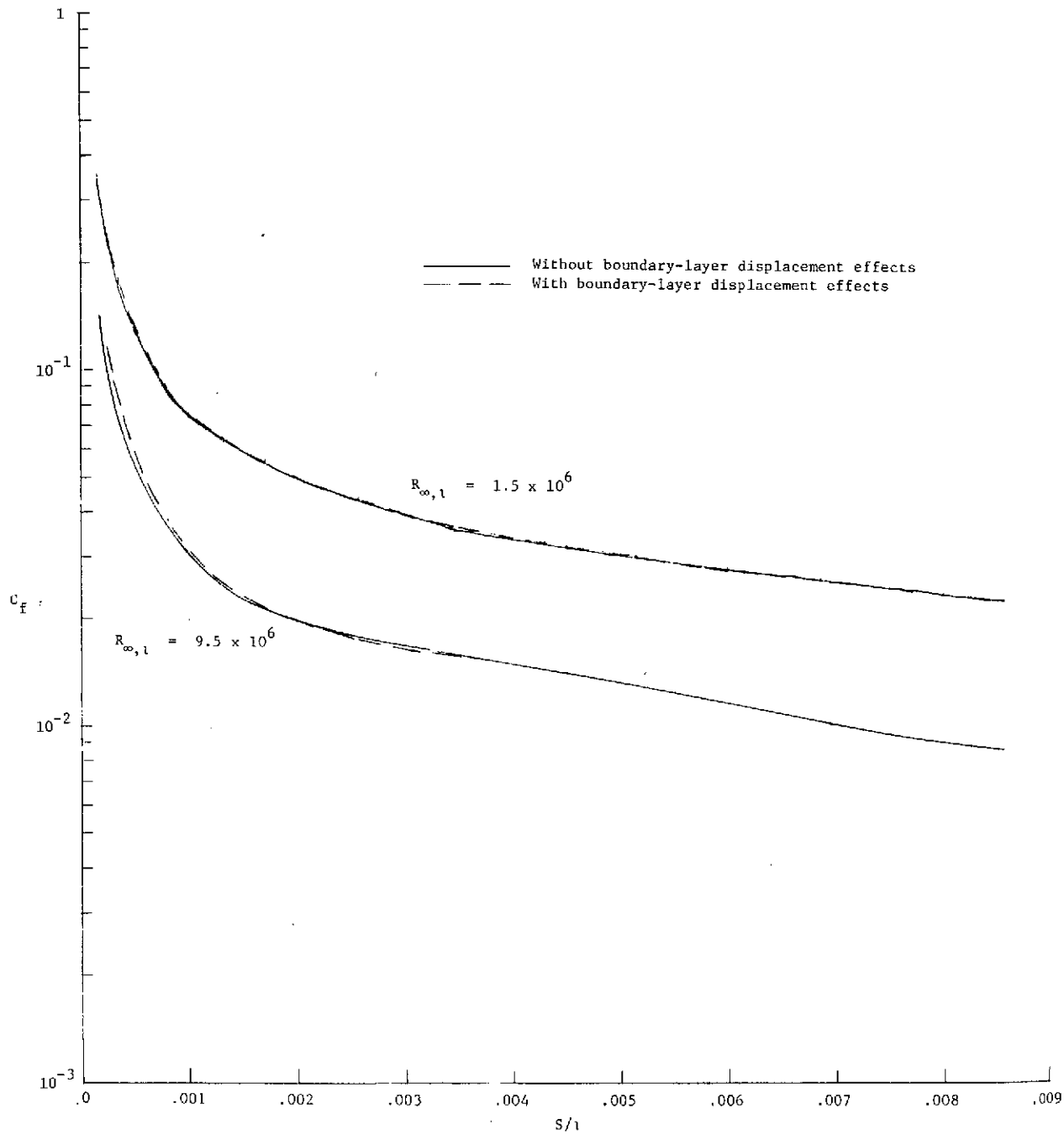

(c) n = 0.60.

Figure 10.- Continued.

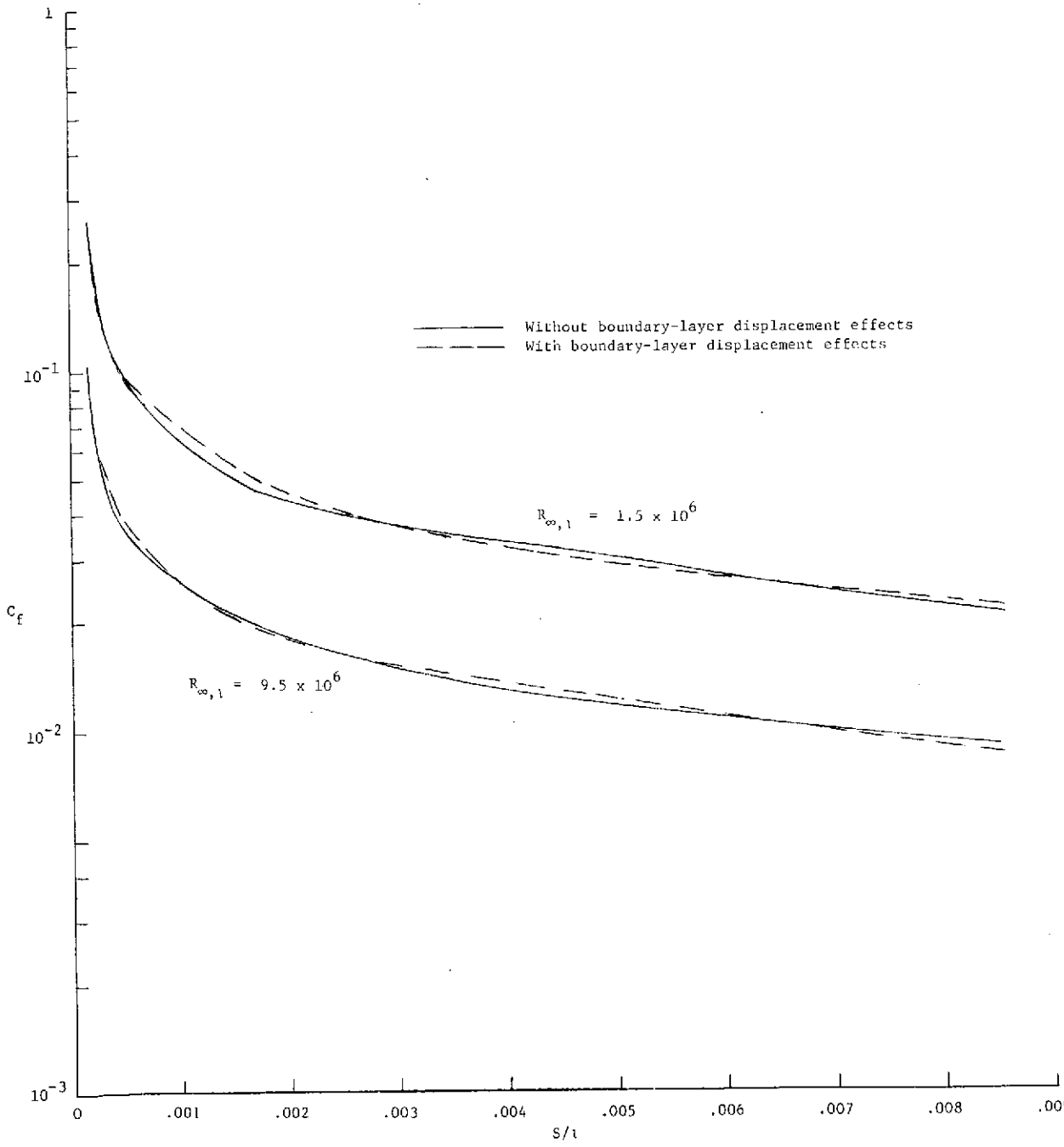

(d) n = 0.667.

Figure 10.- Continued.

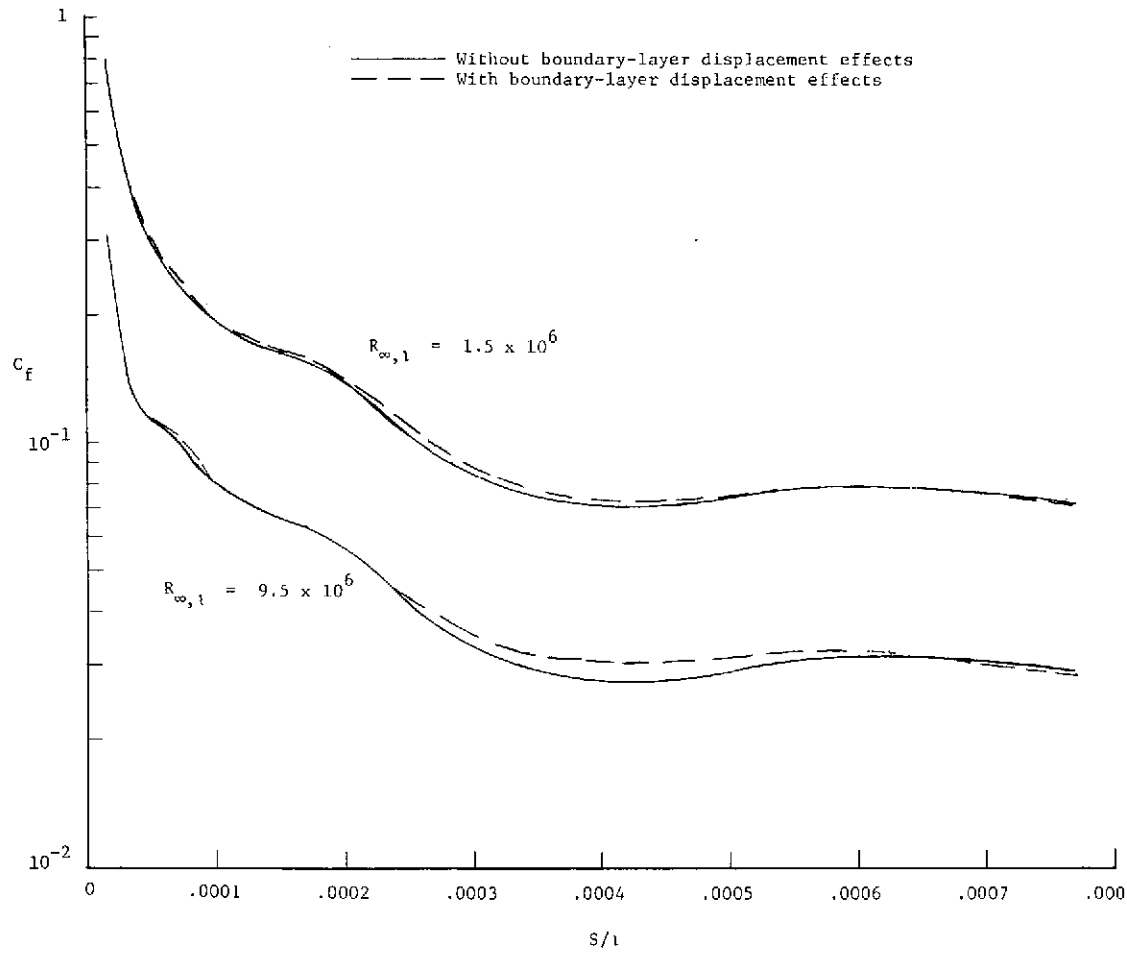

(e) n = 0.75.

Figure 10.- Continued.

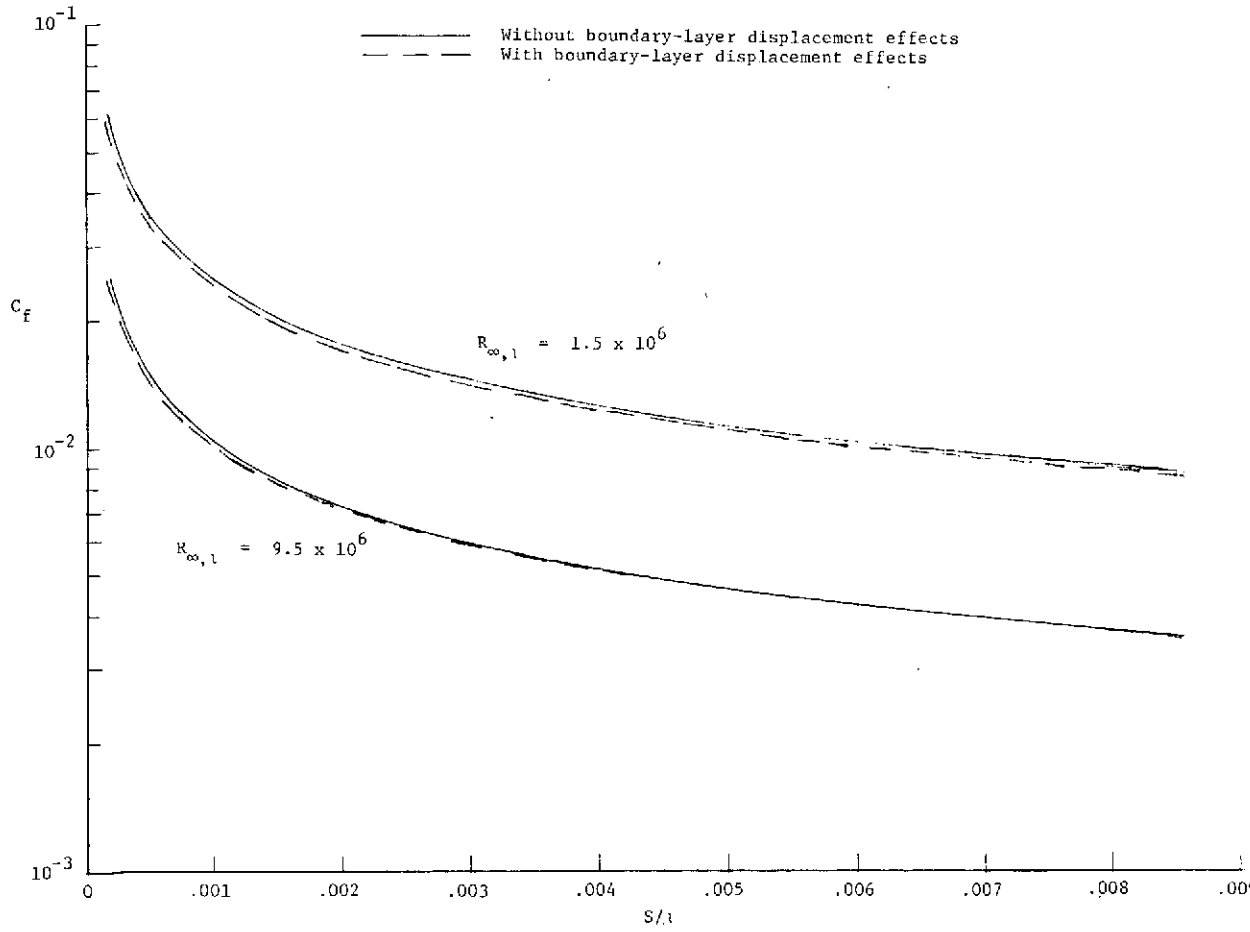

(f) n = 1.00.

Figure 10.- Concluded.

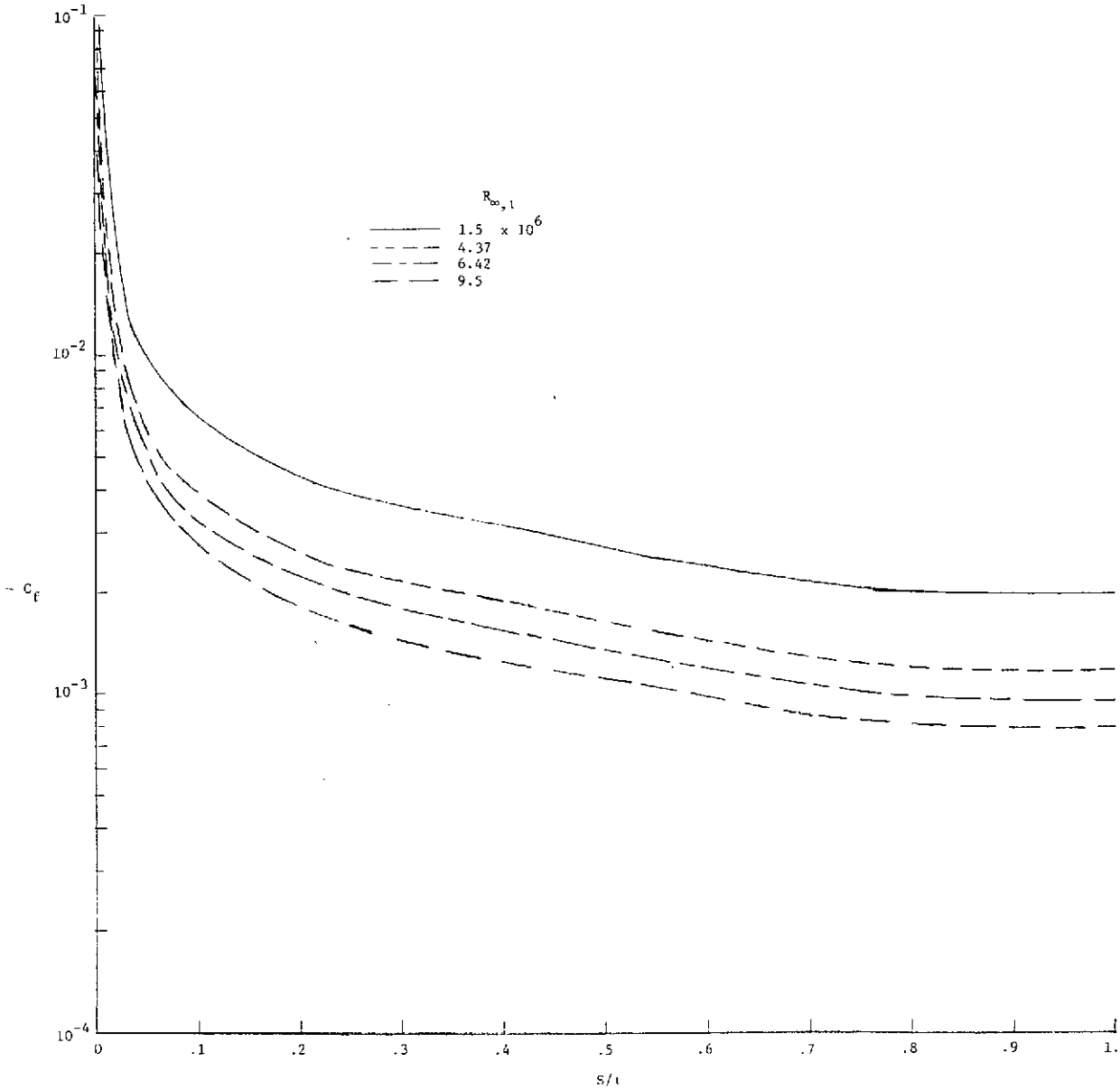

(a) n = 0.25.

Figure 11.- Variation of local skin-friction coefficient along body surface for four Reynolds numbers. Tick marks locate beginning of transition.

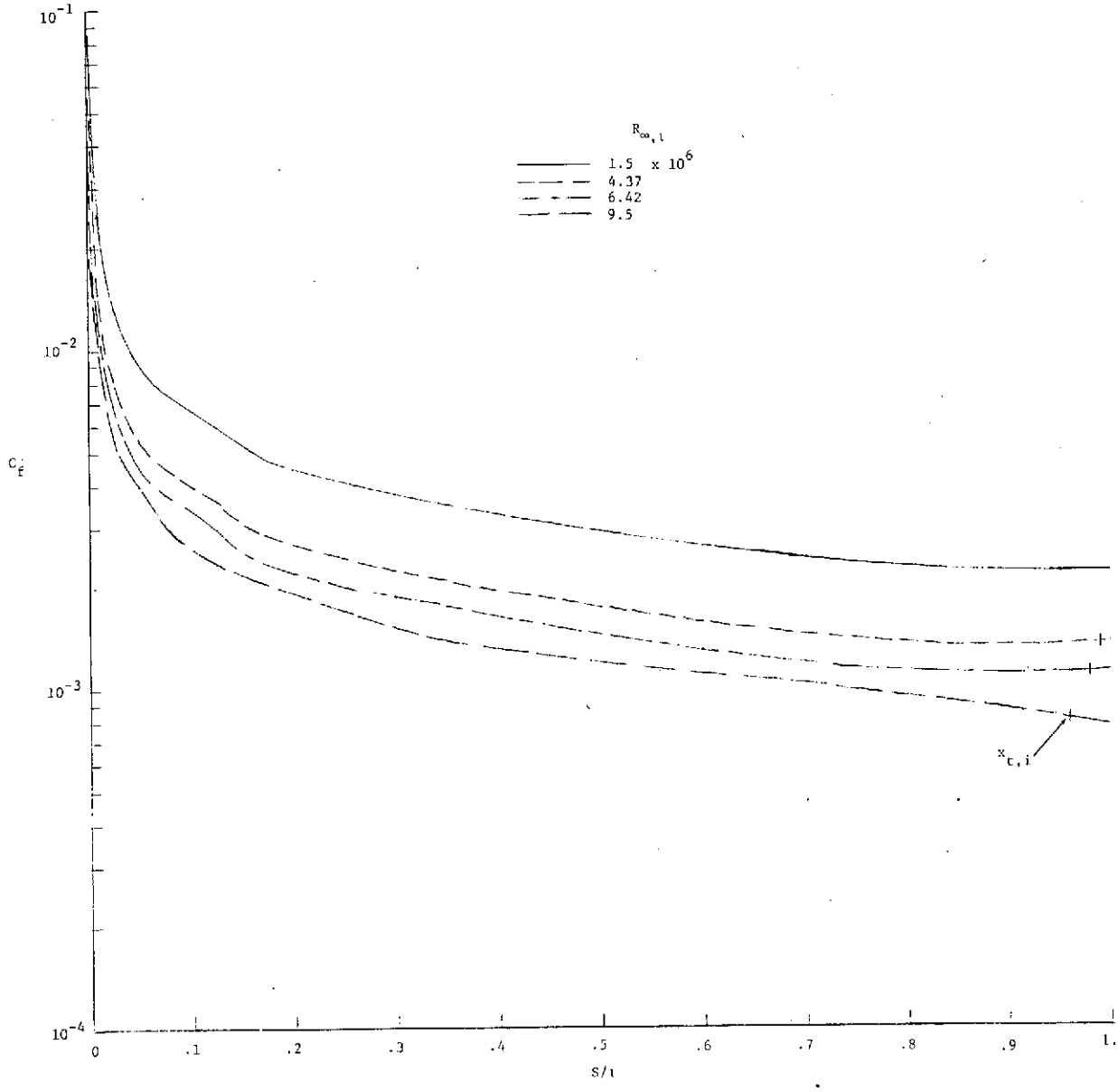

(b) n = 0.50.

Figure 11.- Continued.

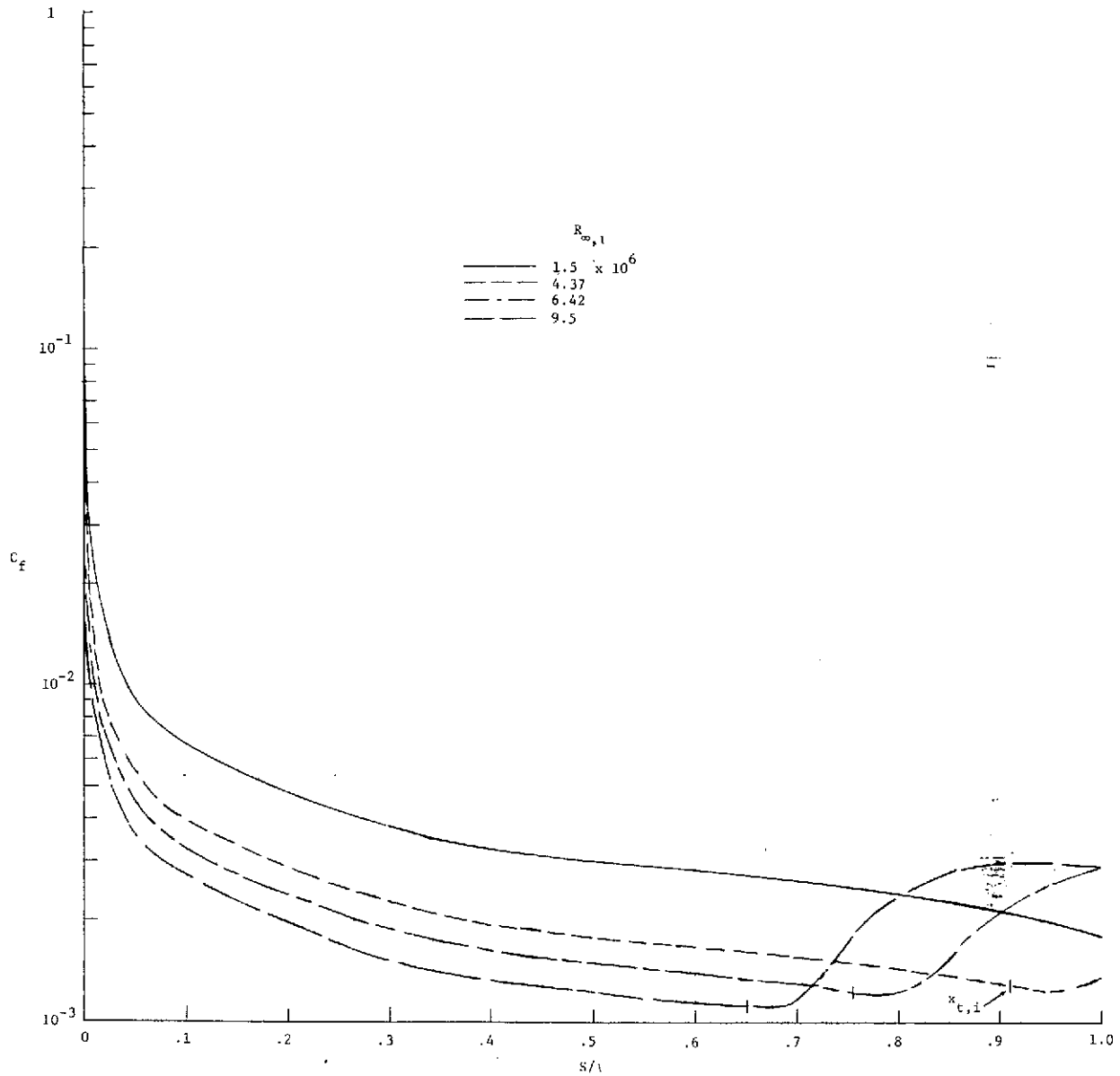

(c) n = 0.60.

Figure 11.- Continued.

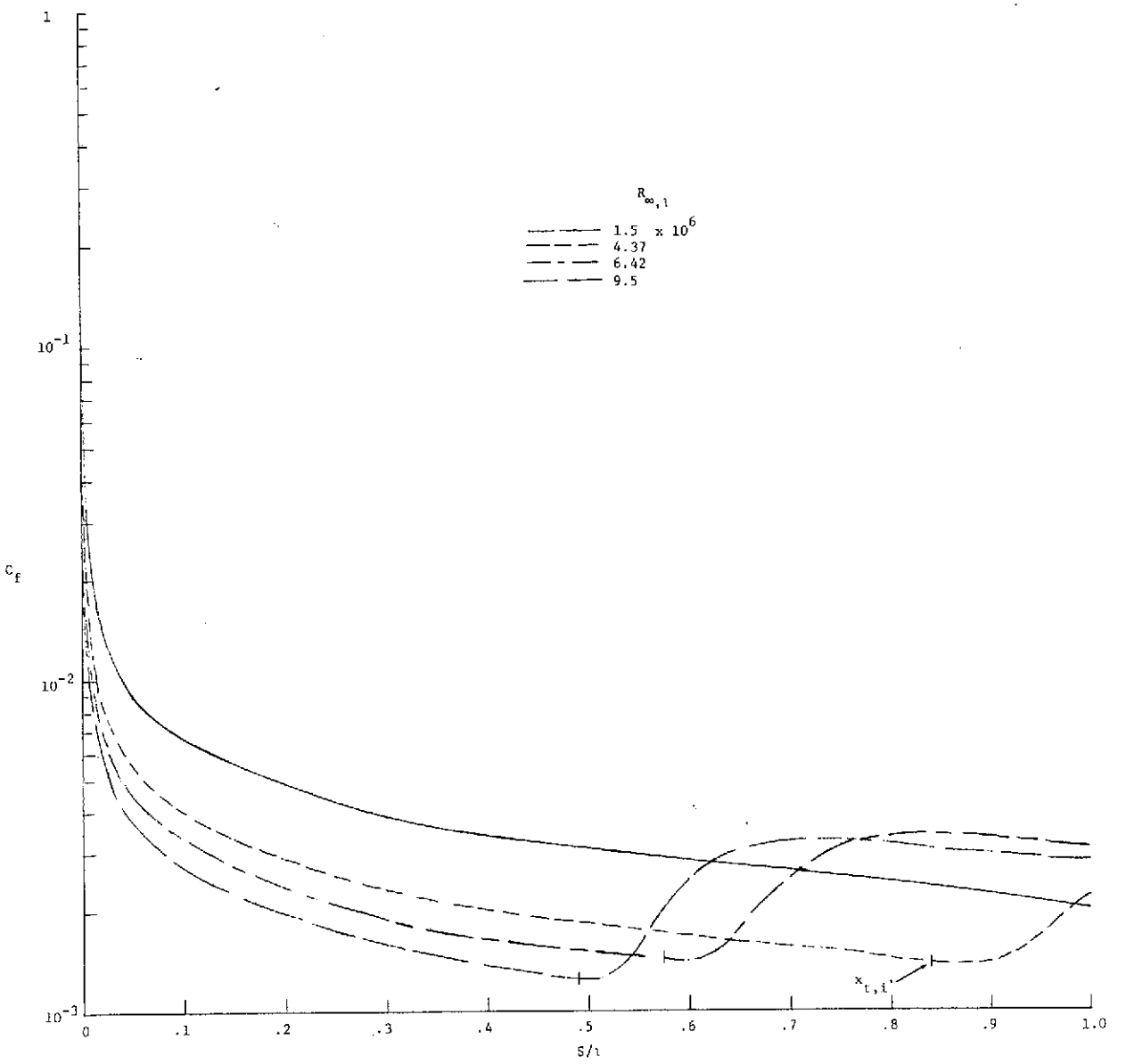

(d) n = 0.667.

Figure 11.- Continued.

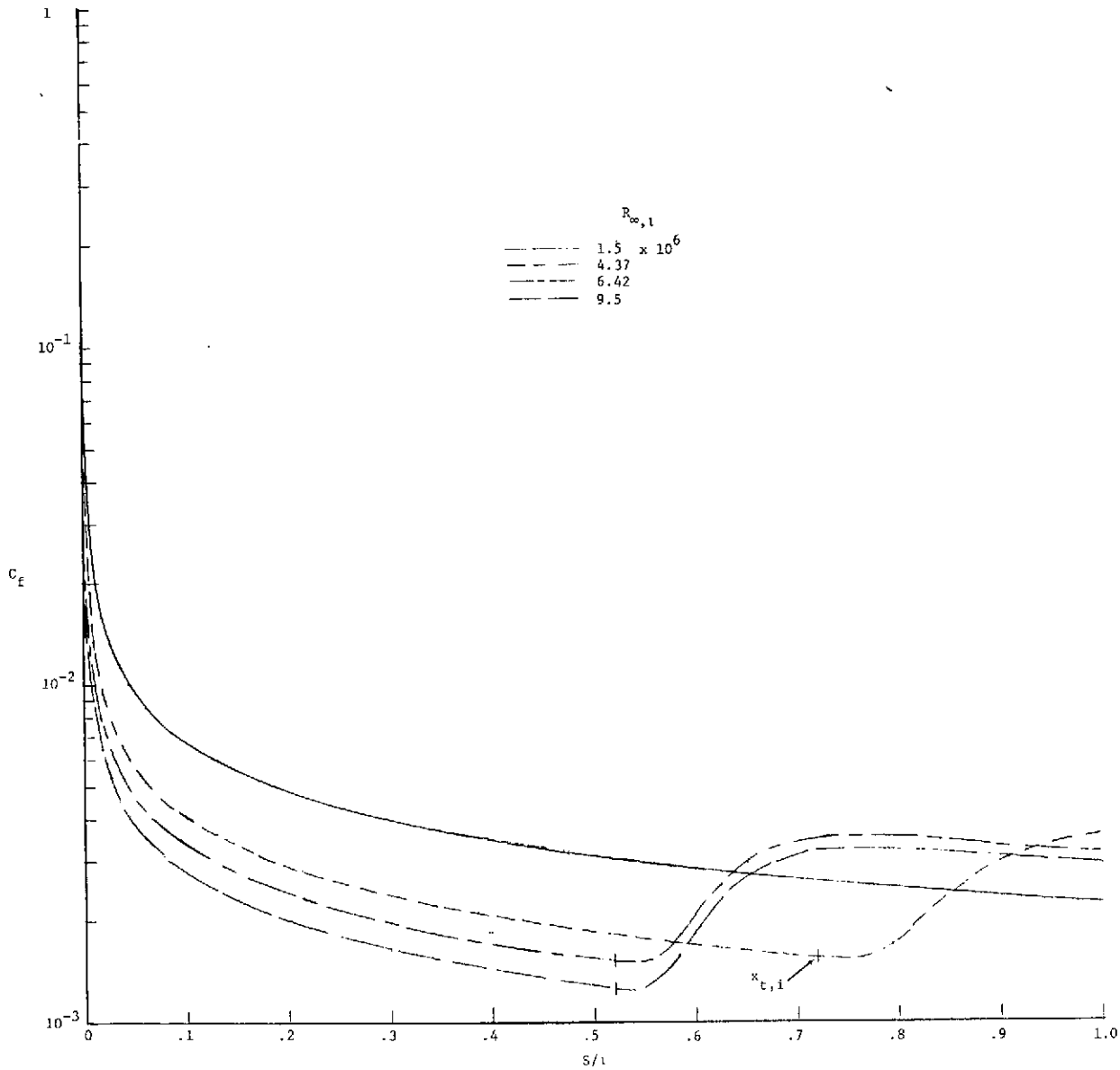

(e) n = 0.75.

Figure 11.- Continued.

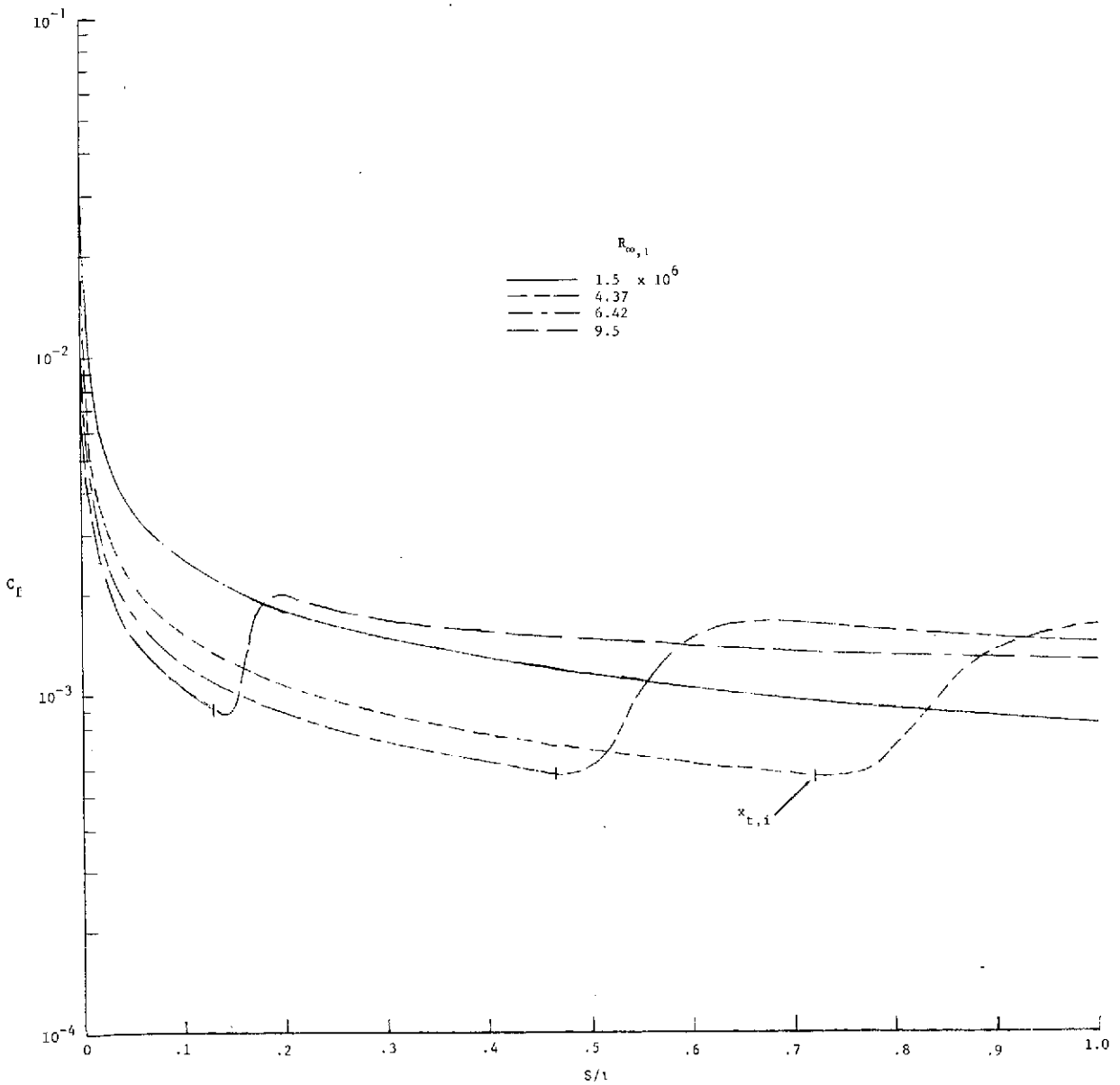

(f) n = 1.00.

Figure 11.- Concluded.

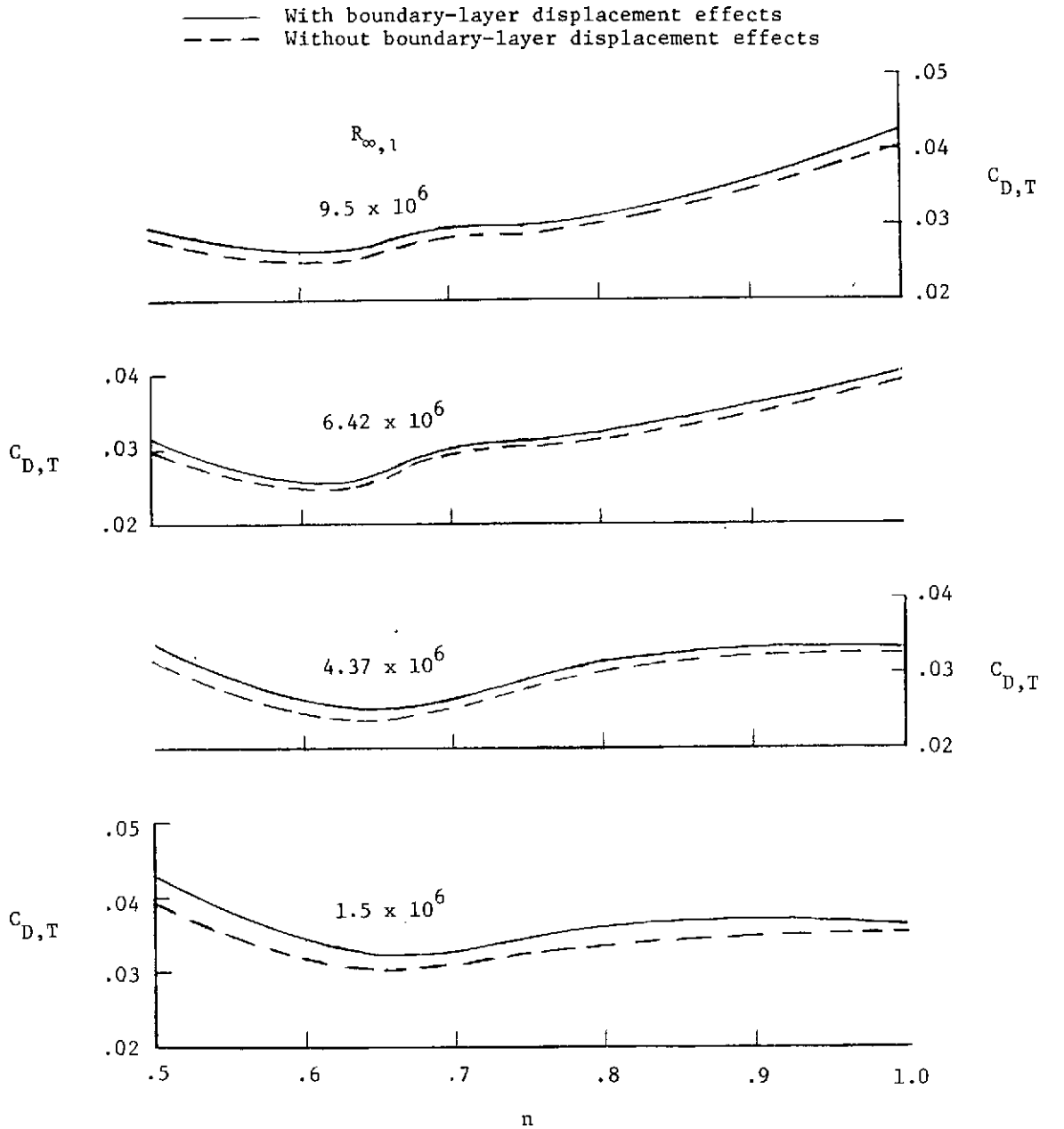

(a) Total drag.

Figure 12.- Comparison of drag coefficients computed with and without boundary-layer displacement effects.

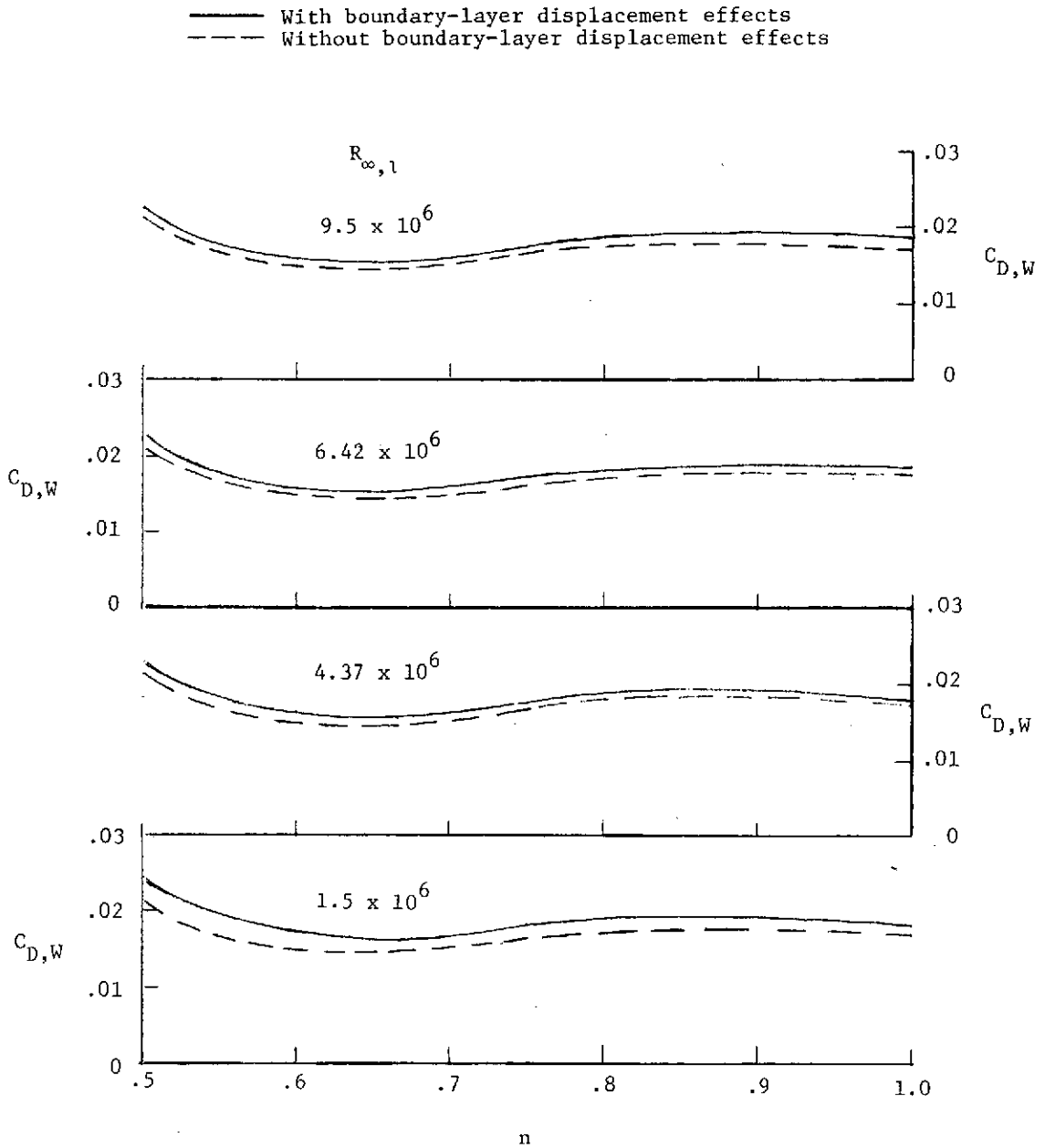

(b) Wave drag.

Figure 12.- Continued.

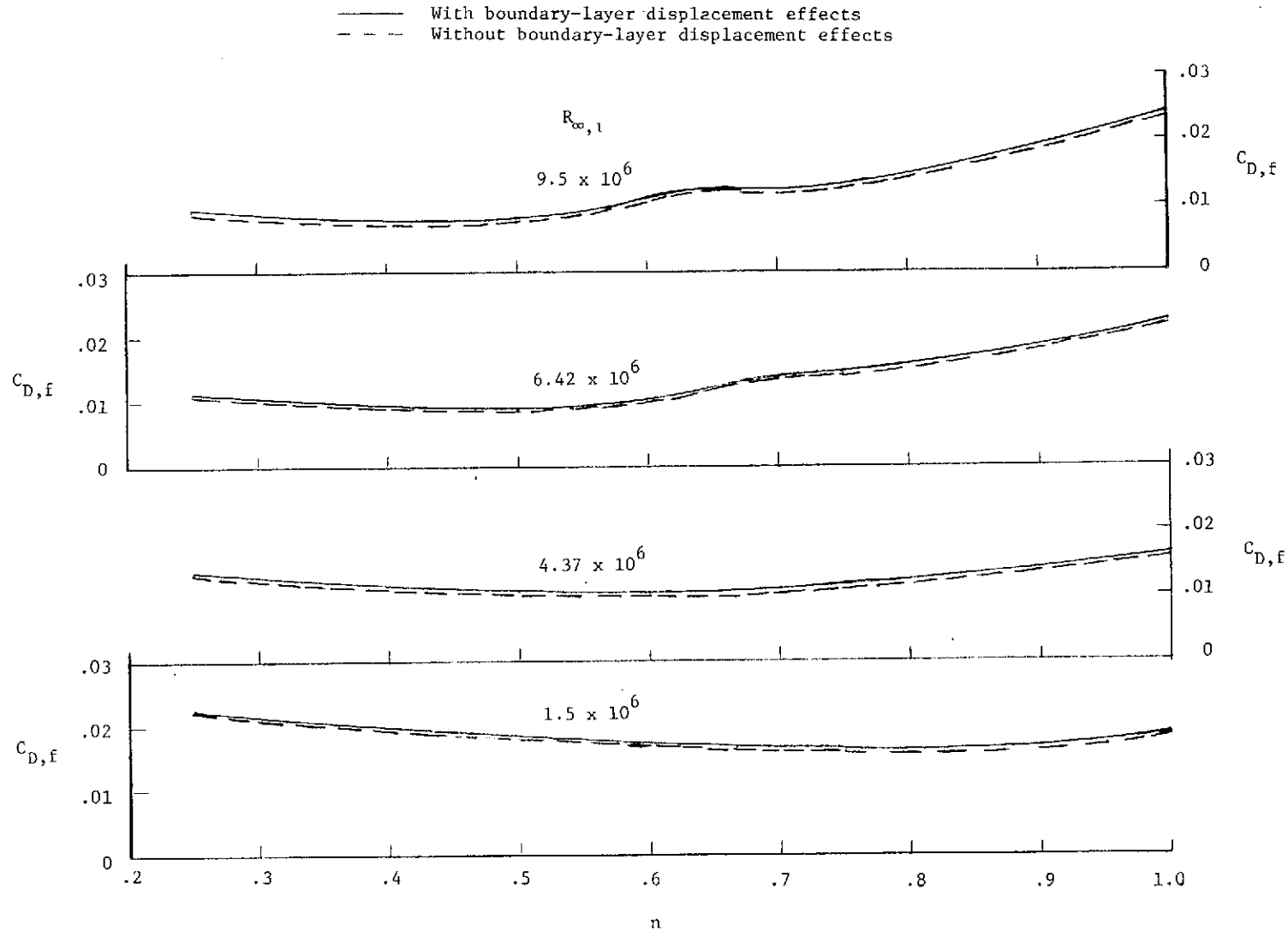

(c) Skin friction.

Figure 12.- Concluded.

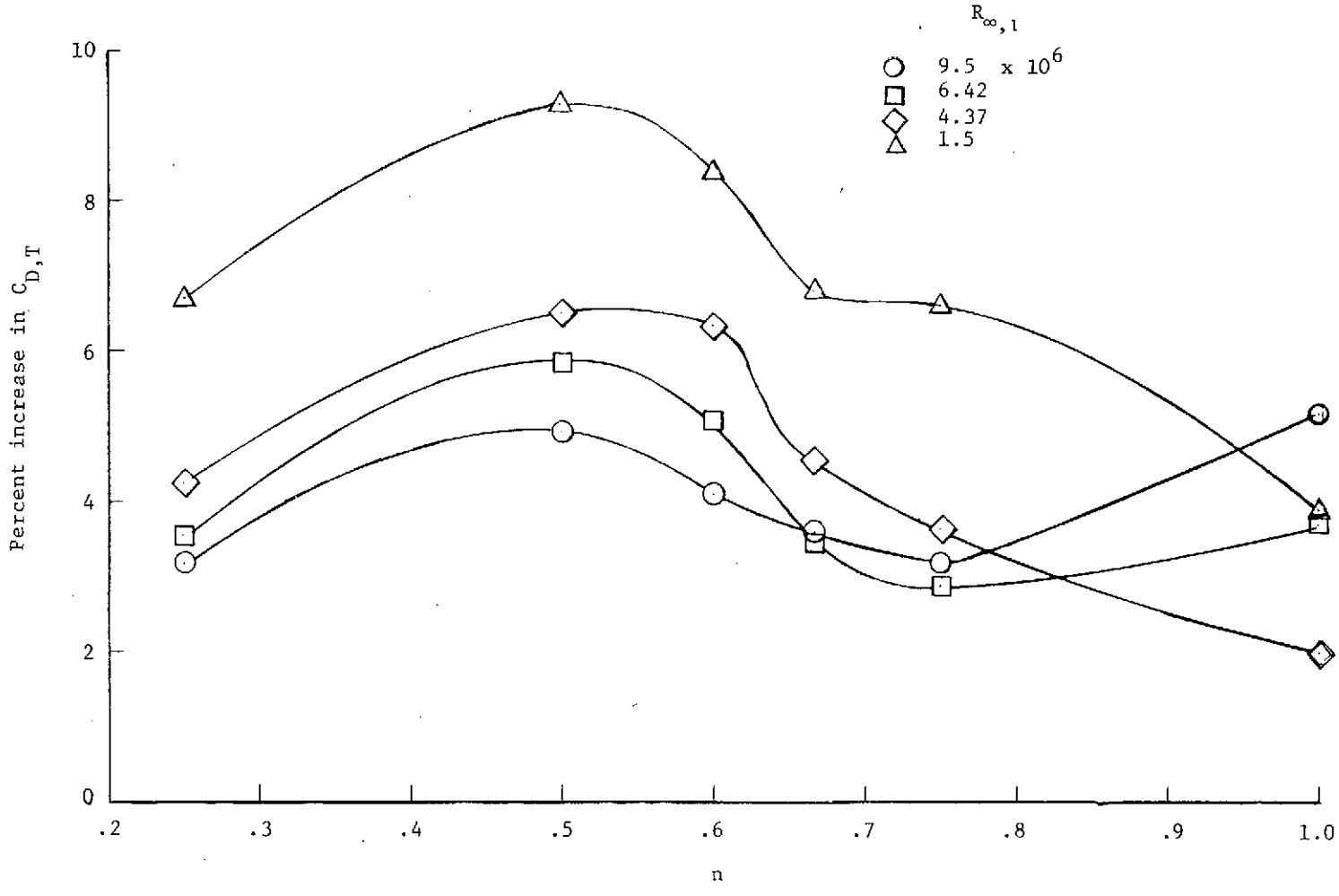

(a) Total drag.

Figure 13.- Percent increase in calculated-drag coefficients due to boundary-layer displacement effects.

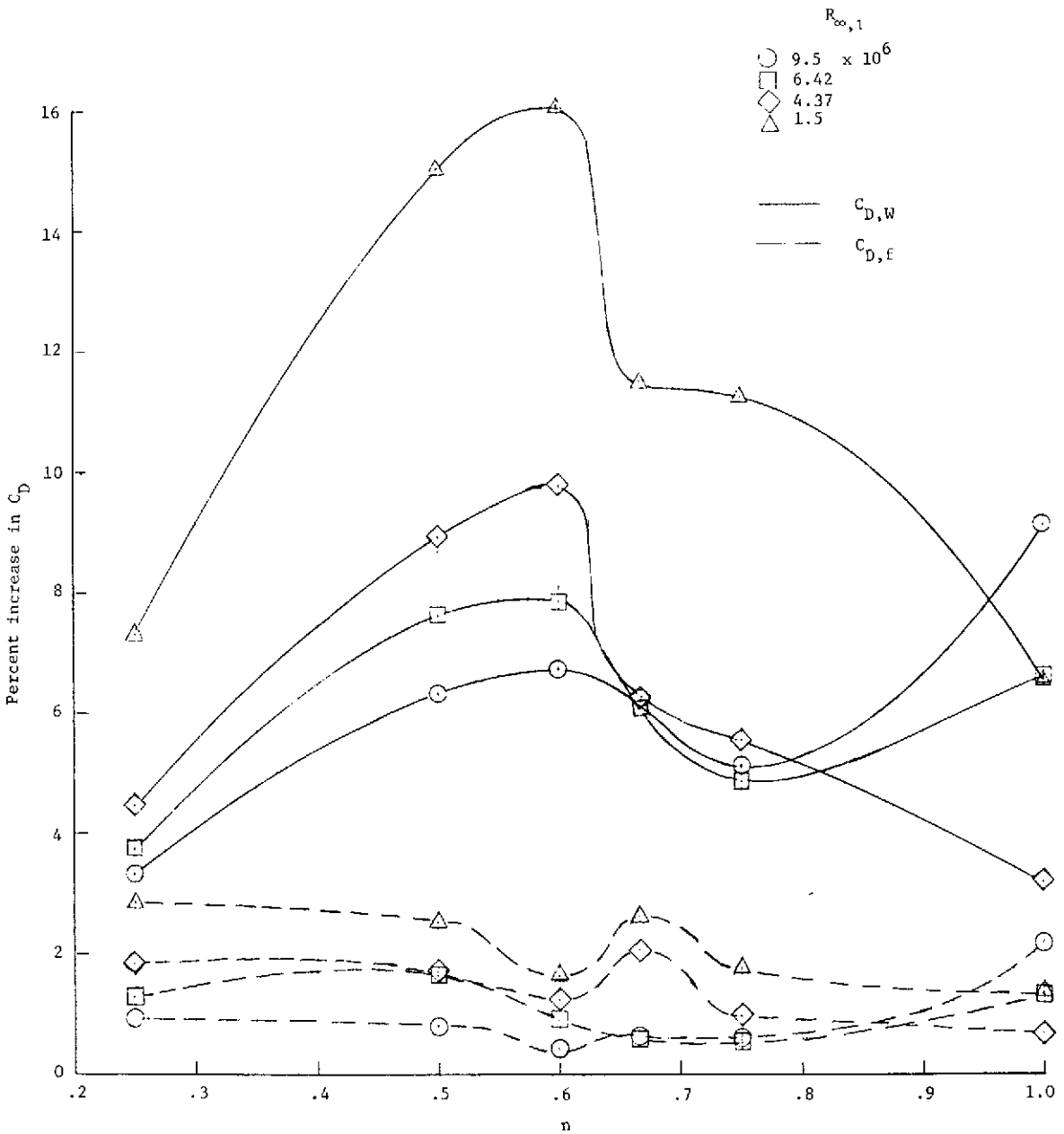

(b) Wave and skin-friction drag.

Figure 13.- Concluded.

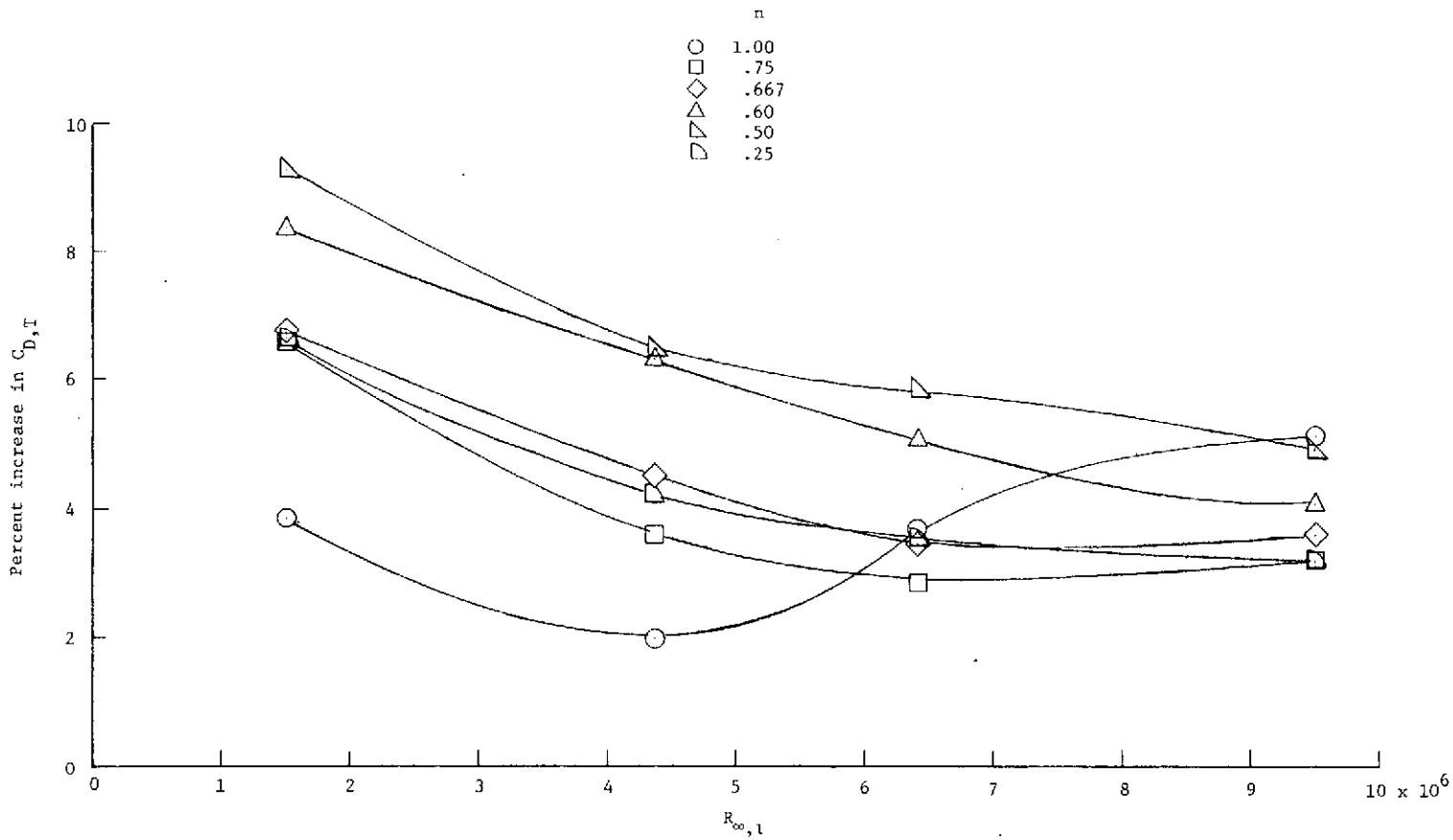

(a) Total drag.

Figure 14.- Percentage increase in drag coefficient for six bodies due to boundary-layer displacement thickness as function of Reynolds number.

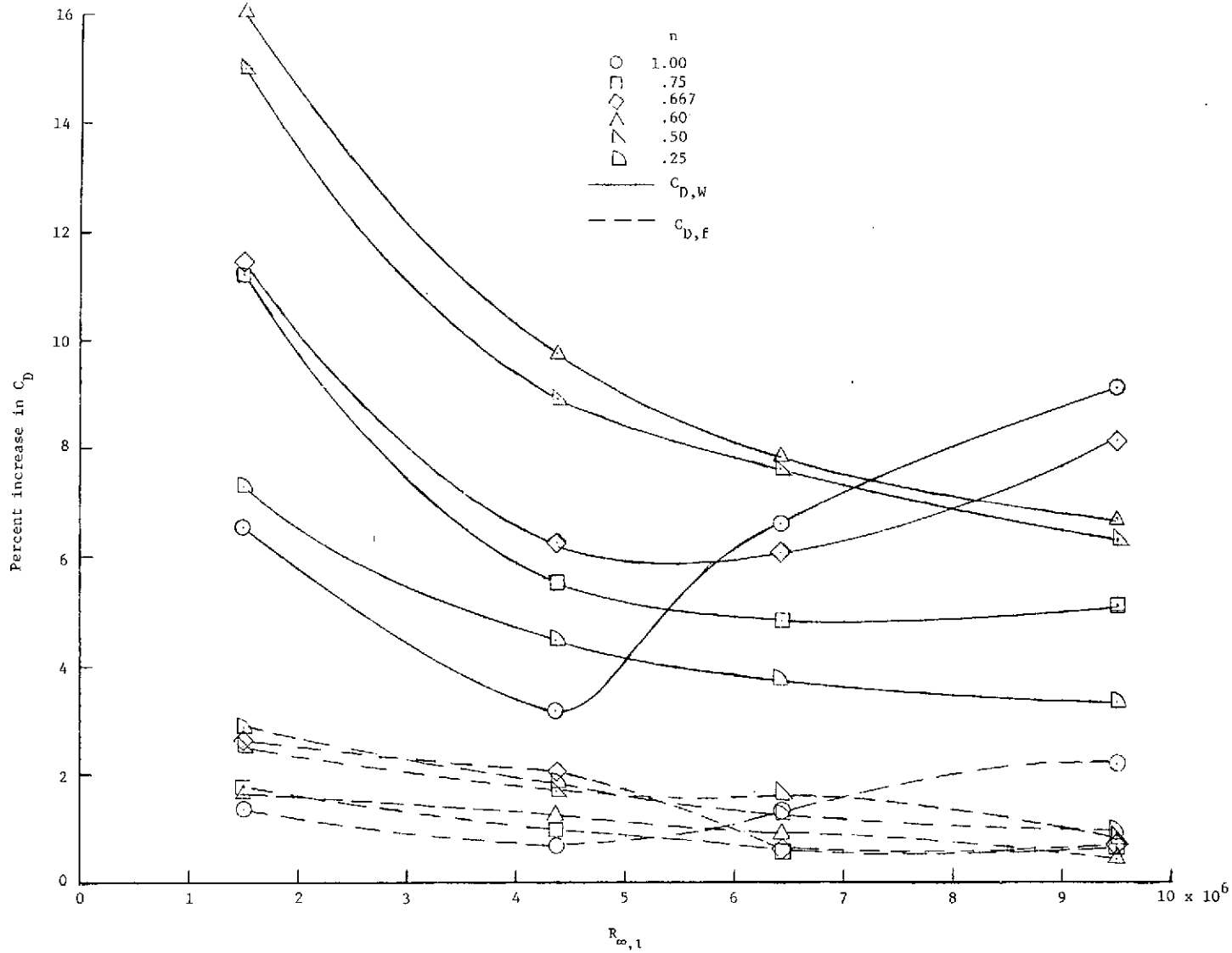

(b) Wave and skin-friction drag.

Figure 14.- Concluded.

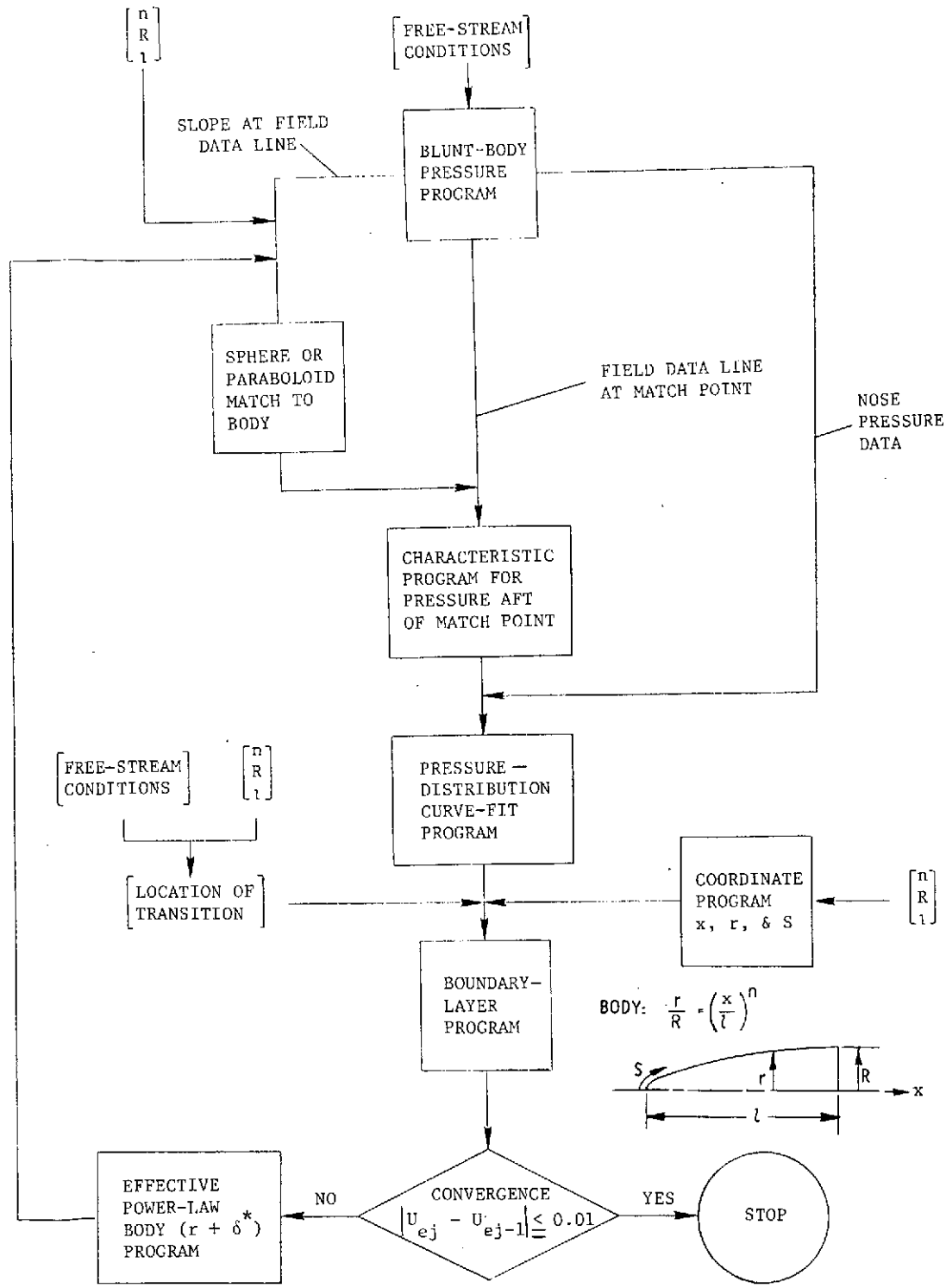

Figure 15.- Calculation procedure for iteration of boundary-layer displacement-thickness effects on wave and skin-friction drag for power-law bodies.

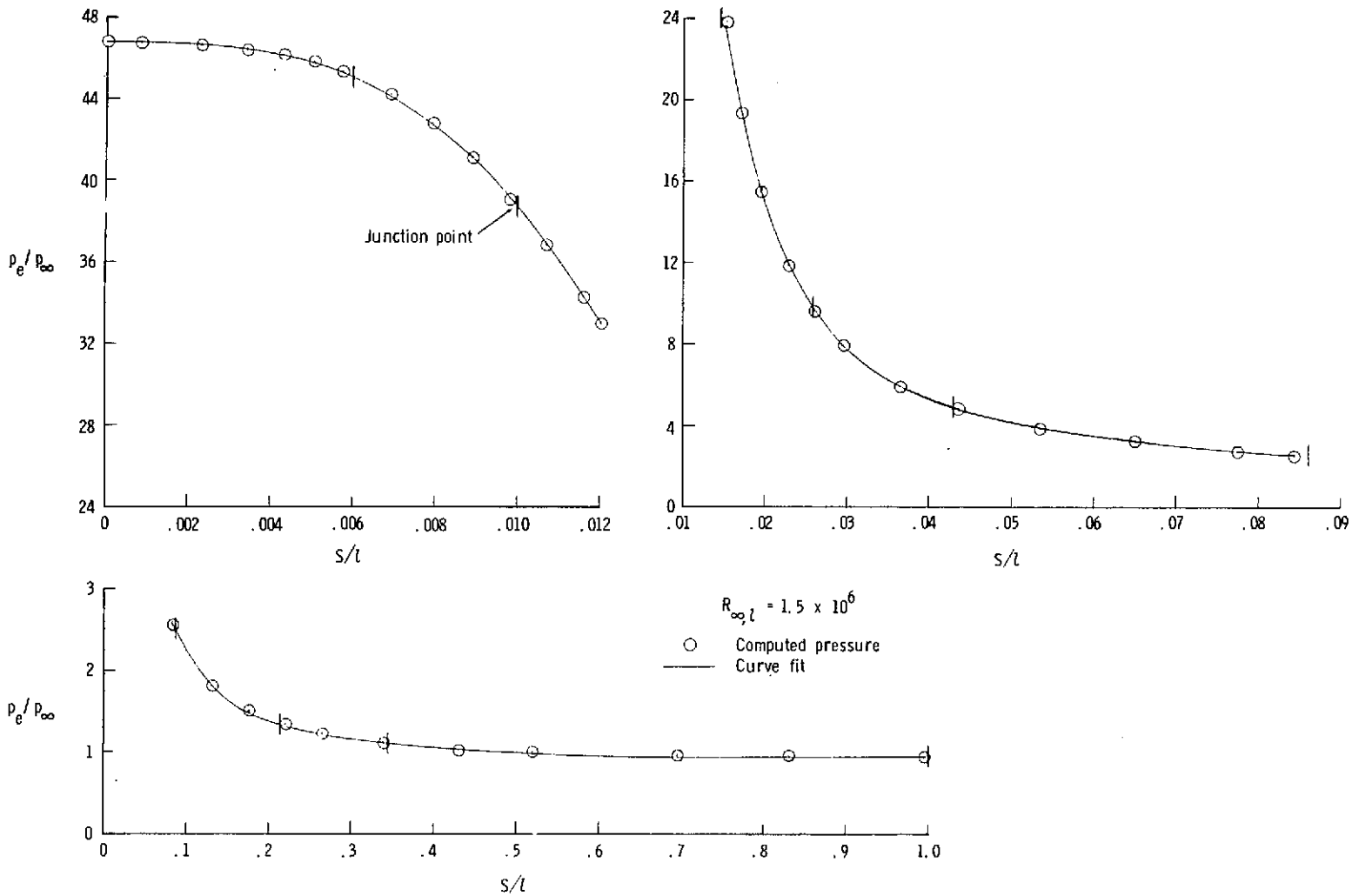

(a) n = 0.25.

Figure 16.- Typical spline function curve fits of computed pressure distributions. Tick marks identify curve-fit junction points.

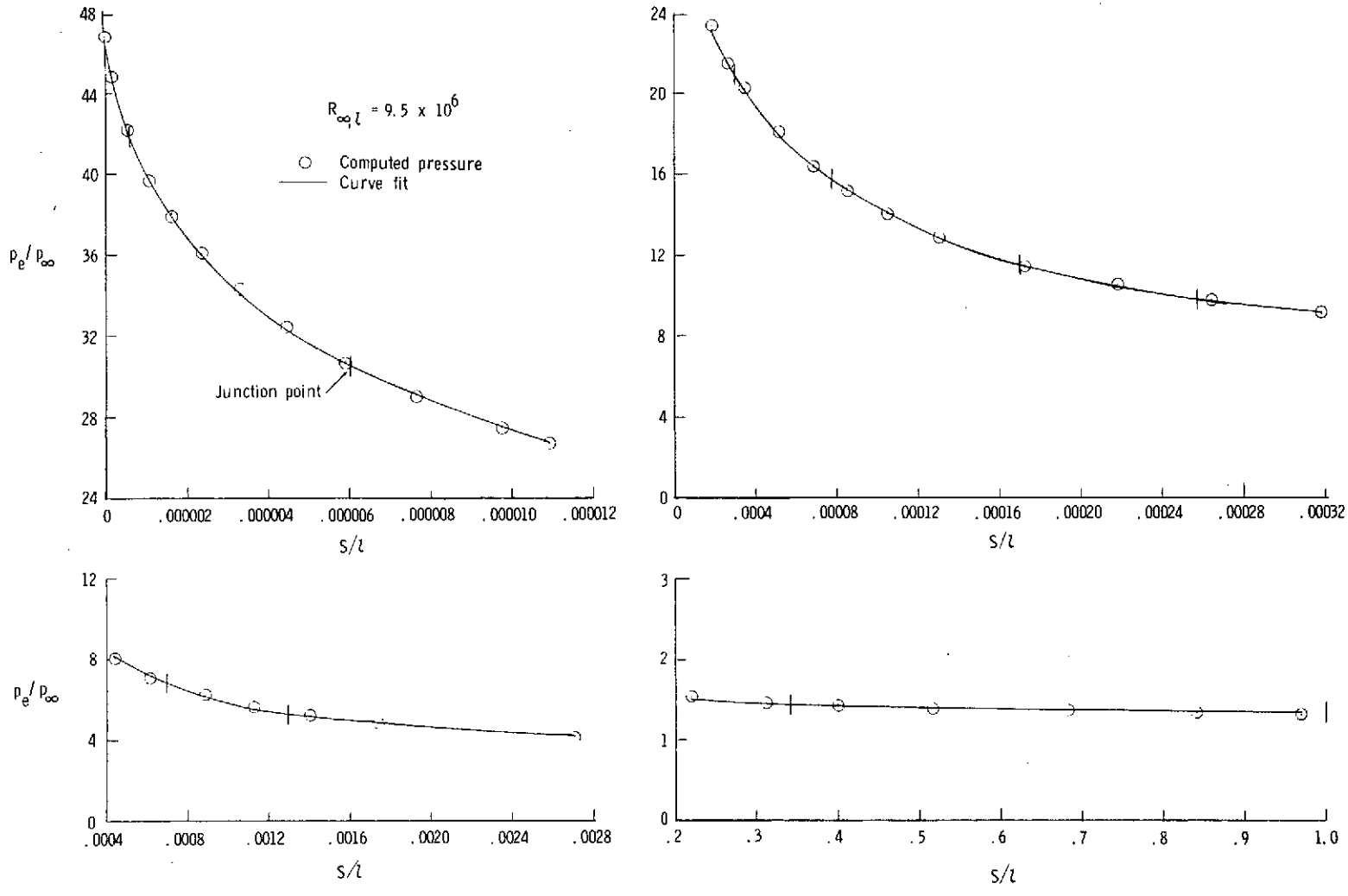

(b) n = 0.75.

Figure 16.- Concluded.

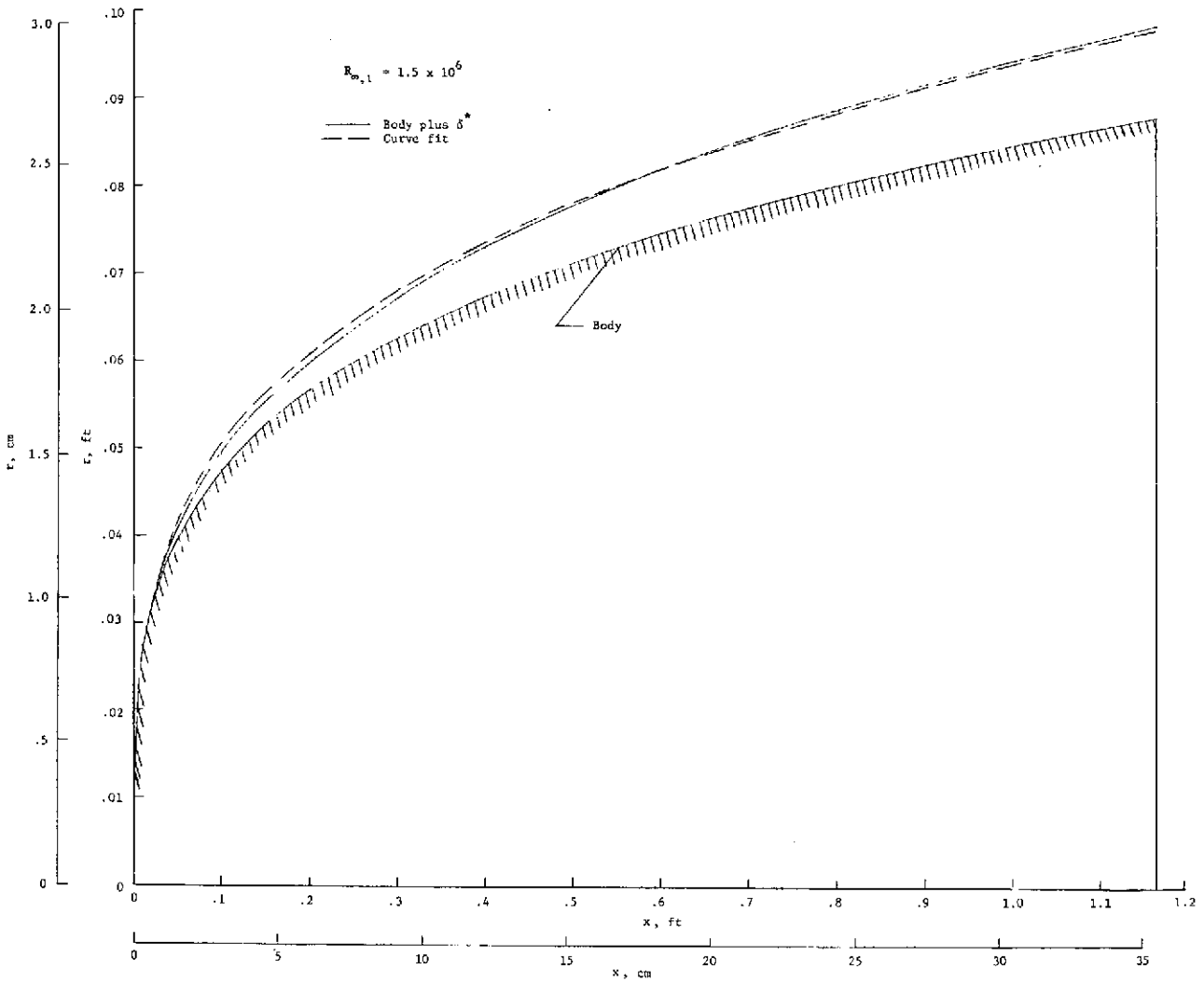

(a) n = 0.25

Figure 17.- Examples of effective power-law body representations of basic body plus boundary-layer displacement thickness.

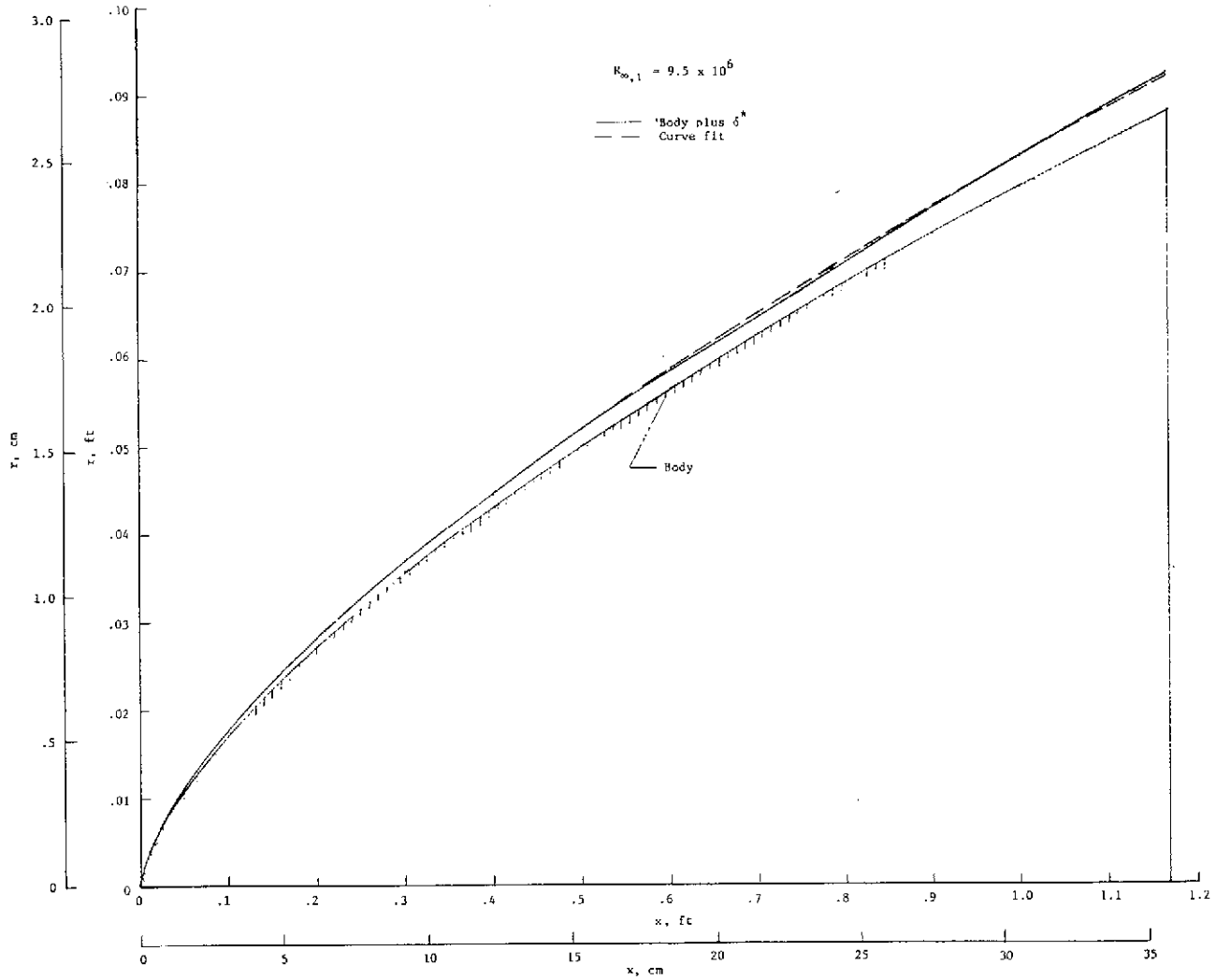

(b) n = 0.667.

Figure 17.- Continued.

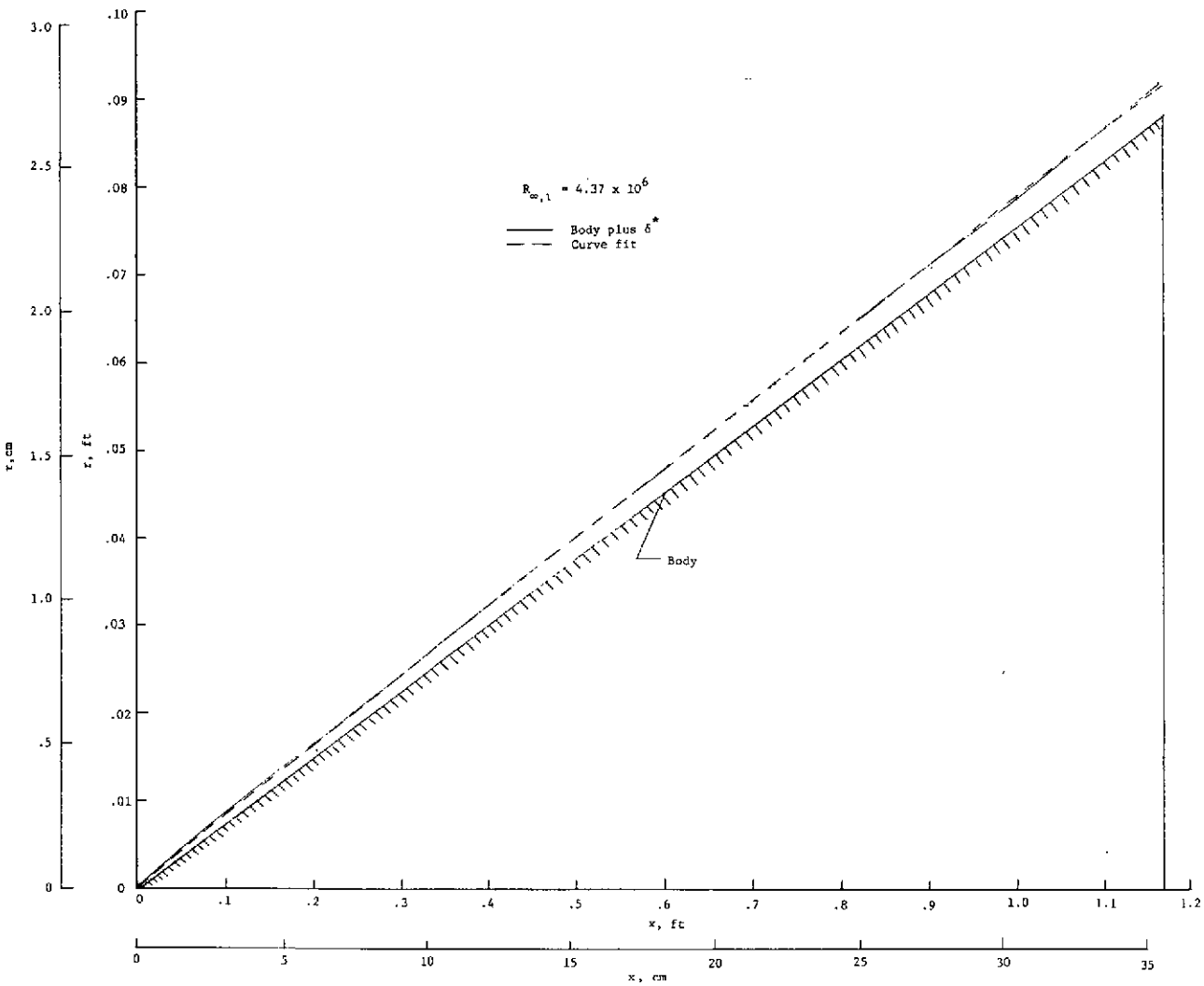

(c) n = 1.00.

Figure 17.- Concluded.